Cement and Concrete Composites 107 (2020) 103493

Contents lists available at ScienceDirect

Cement and Concrete Composites

journal homepage: http://www.elsevier.com/locate/cemconcomp

Using particle composition of fly ash to predict concrete strength and electrical resistivity

Taehwan Kim [a,*], M. Tyler Ley [b], Shinhyu Kang [b], Jeffrey M. Davis [c], Seokhyeon Kim [a], Pouya Amrollahi [b]

[a] School of Civil and Environmental Engineering, University of New South Wales, Sydney, NSW, 2052, Australia
[b] Department of Civil and Environmental Engineering, Oklahoma State University, Stillwater, OK, 74078, USA
[c] EOS GmbH, Lise-Meitner-Strasse 7, D-82216 Maisach, Germany

ARTICLE INFO

Keywords:
Fly ash
Particle characterization
SEM-EDS
Concrete
Classification
Sustainability

ABSTRACT

This paper uses a new approach where fly ash is characterized on a particle-by-particle basis using automated scanning electron microscopy. The particle data is then analyzed with principal component analysis (PCA) to find interrelationships among the particle chemical composition for 20 different fly ashes. Consistent trends were observed in 20 fly ashes. These trends from PCA were verified by making comparisons of these trends for individual particles. One application is introduced using this particle data. Each particle is categorized into four broad groups with a limited chemical composition. These four groups were found in different proportions in the different fly ashes investigated. Compressive strength and surface electrical resistivity were measured from concrete mixtures made with these fly ashes and the four groups correlated with the performance in concrete. This finding is an important step to develop a more general classification of fly ash based on the individual particle make-up, which helps to optimize the mixture design and also benefits the sustainable concrete by increasing the effectiveness of industrial by-waste usage.

1. Introduction

Fly ash is a by-product of the combustion processes of pulverized coal. Fly ash collected from a dust-collection system is typically composed of finely divided spherical particles with a diameter of 1 μm–150 μm [1–3]. The major oxide components of fly ash are SiO_2, Al_2O_3, Fe_2O_3, and CaO with minor oxides, including MgO, Na_2O, K_2O, SO_3, SrO, TiO_2, MnO, and P_2O_5 [3–8]. Fly ash has been used in a wide range of applications including: a low-cost adsorbent for flue gas cleaning and wastewater treatment, a raw material for synthesis of geopolymers and zeolites, a supplementary cementitious material (SCM) in concrete, a backfill material in mining, and roadway soil stabilization [3,5,8–10].

Fly ash is a waste material from the point of view of the power generation. However, because of the good performance and economic and environmental benefits of fly ash in concrete, the demand has grown steadily [5,6]. Over 98% of the ready mix concrete companies in the United States have used fly ash in concrete [11]. Numerous researchers [12–18] have also shown the potential of the utilization of high volume fly ash in structural applications. However, several challenges still limit its utilization in greater volumes. In particular, inconsistent physical and chemical properties among fly ash sources can lead to different performance when blended in concrete [2,19–21]. Though the demand for fly ash as an SCM is increasing, it is still difficult to predict the performance of fly ash in concrete, including mechanical performance and durability properties [2,19–21]. Comprehensive characterization methods that are rapid and correlate with performance in concrete can significantly improve the optimization of the mixture design and thus offer opportunities for reducing the environmental impact of concrete.

The reactivity of fly ash has been historically determined by using bulk characterization methods such as X-ray fluorescence (XRF), X-ray diffraction (XRD), and leaching tests [2,22–25]. Classification methods based on the bulk chemistry are widely used in ASTM C618 [26] and EN 450 [27]. These classifications can provide general insights but they are not useful to predict the performance of the fly ash in concrete. For example, ASTM C618 defines two classes of fly ash: Class F and Class C. However, ASTM C618 explicitly mentioned that the bulk chemical component determinations do not predict the performance of the fly ash

* Corresponding author.
E-mail address: taehwan.kim@unsw.edu.au (T. Kim).

https://doi.org/10.1016/j.cemconcomp.2019.103493
Received 3 September 2019; Received in revised form 6 December 2019; Accepted 20 December 2019
Available online 31 December 2019

Table 1
Chemical composition of fly ashes (C: Class C fly ash and F: Class F fly ash).

Fly ash		Chemical composition (% by mass)											
		SiO_2	Al_2O_3	Fe_2O_3	CaO	MgO	SO_3	Na_2O	K_2O	TiO_2	P_2O_5	SrO	LOI[a]
C1	XRF	38.4	19.8	6.2	21.9	5.3	1.4	1.8	0.6	1.4	1.7	0.4	0.4
	ASEM	32.2	22.1	6.3	25.6	5.9	1.0	3.1	0.9	1.0	1.7	0.2	–
C2	XRF	36.2	19.9	6.7	24.0	5.2	1.4	1.7	0.5	1.4	1.4	0.4	0.2
	ASEM	35.8	19.2	5.6	26.9	5.5	1.0	3.0	0.9	0.7	1.2	0.2	–
C3	XRF	33.2	17.0	5.8	28.1	7.0	1.9	1.9	0.4	1.4	1.4	0.4	0.9
	ASEM	25.3	19.3	5.2	32.5	7.8	2.6	3.4	0.6	1.1	1.9	0.3	–
C4	XRF	37.6	23.2	5.5	21.8	4.2	1.0	1.7	0.6	1.6	1.6	0.4	0.2
	ASEM	29.9	24.5	5.3	26.2	4.9	1.4	3.0	0.8	1.4	1.7	0.9	–
C5	XRF	37.9	19.5	5.7	22.9	5.6	0.9	2.0	0.5	1.4	1.5	0.4	1.2
	ASEM	27.8	20.8	5.9	31.4	7.0	0.6	2.9	0.5	0.8	1.9	0.4	–
C6	XRF	37.0	20.6	5.3	15.6	3.6	2.9	9.2	0.7	1.3	0.7	0.7	0.7
	ASEM	35.1	23.3	3.0	15.0	4.0	2.0	13.4	0.6	1.1	1.6	0.9	–
C7	XRF	39.1	20.0	6.2	22.3	4.9	1.0	1.8	0.7	1.4	1.1	0.4	0.4
	ASEM	32.6	21.5	5.9	25.6	5.2	0.9	3.6	1.1	1.0	1.5	1.1	–
C8	XRF	40.0	20.9	5.9	21.5	5.0	0.8	1.6	0.7	–	–	–	0.2
	ASEM	40.1	22.6	4.5	19.4	5.7	0.8	3.7	0.9	0.6	1.4	0.1	–
C9	XRF	36.0	22.4	5.5	24.0	4.8	1.2	1.7	0.5	–	–	–	0.1
	ASEM	31.5	24.0	6.0	25.7	5.3	1.0	3.7	0.6	0.9	1.1	0.1	–
C10	XRF	35.9	18.0	6.7	25.8	6.1	1.8	1.8	0.4	1.2	0.8	0.5	0.2
	ASEM	36.0	19.3	5.1	22.7	7.8	2.0	4.7	0.6	1.0	0.3	0.5	–
F1	XRF	56.3	20.1	5.7	10.3	3.0	0.5	0.6	1.4	1.2	0.1	0.3	0.2
	ASEM	45.2	24.3	6.6	14.7	3.5	0.8	1.8	1.9	0.7	0.2	0.2	–
F2	XRF	52.0	16.4	4.4	18.7	2.9	0.9	0.8	0.9	1.0	0.3	0.2	1.2
	ASEM	50.4	20.9	3.9	17.1	3.7	0.5	1.0	1.4	0.7	0.1	0.3	–
F3	XRF	59.2	24.4	6.2	4.0	1.2	0.4	1.4	1.1	1.1	0.1	0.1	0.6
	ASEM	48.8	26.6	6.6	9.3	2.0	0.3	1.7	1.9	1.5	0.1	1.1	–
F4	XRF	49.7	24.2	4.7	12.9	3.3	0.7	1.0	0.6	1.7	0.5	0.3	0.2
	ASEM	45.3	27.4	4.0	14.6	3.6	0.7	1.5	0.6	1.1	0.4	0.8	–
F5	XRF	51.5	23.2	11.9	3.9	1.1	0.9	0.9	2.4	1.3	0.2	0.1	2.4
	ASEM	53.2	25.4	11.2	2.1	0.2	0.8	1.0	4.4	0.7	0.0	1.0	–
F6	XRF	49.0	20.9	16.1	4.9	0.9	1.6	1.1	2.5	1.1	0.1	0.0	1.8
	ASEM	51.8	25.7	12.3	2.5	0.3	0.7	1.6	4.1	0.7	0.1	0.2	–
F7	XRF	47.7	24.9	14.7	3.7	0.9	0.7	0.7	1.7	1.3	0.3	0.1	2.2
	ASEM	51.9	26.4	8.0	3.3	0.5	1.7	4.0	2.5	0.9	0.6	0.1	–
F8	XRF	56.9	22.6	4.6	7.3	2.3	0.3	1.7	1.2	–	–	–	0.5
	ASEM	56.9	23.9	3.4	6.2	2.1	0.1	4.1	1.7	0.3	1.2	0.1	–
F9	XRF	53.5	19.2	6.3	13.2	3.1	0.6	0.6	1.1	–	–	–	0.4
	ASEM	48.3	25.0	5.8	12.6	3.3	0.5	1.3	1.8	1.1	0.2	0.1	–
F10	XRF	57.7	24.5	4.1	8.1	2.0	0.3	0.2	0.9	–	–	–	0.5
	ASEM	53.6	27.8	2.8	10.5	2.5	0.5	0.3	1.3	0.4	0.3	0.0	–

[a] Loss on ignition.

with hydraulic cement in concrete. Despite the benefits of the bulk chemistry one drawback of bulk chemistry is that it is simply the average of the system and cannot consider the complexity of the individual particles. Each particle of fly ash may have a different chemical composition or a combination of crystalline and amorphous materials [28–31].

Fly ash is airborne particles that are created by rapidly cooling the residues of coal combustion in air. During this process, fly ash particles actually created through complex procedures including combustion, melting, and solidification [24,32]. Therefore, the study of the individual particles may provide some insight into this process. Numerous researchers reported that certain glass phases in fly ash are associated with different levels of reactivity [21,33–38]. Several studies have tried to find unique chemical groups of glassy phases by using scanning electron microscopy with electron dispersive spectrometry (SEM-EDS) to examine polished sections of thousands of fly ash particles [21,33,38]. Recently, Durdziński et al. [33] suggested that fly ashes are mainly composed of four groups of chemical glasses after investigating 4 fly ashes [3 Class C fly ashes and 1 Class F fly ash]: i) silicate, ii) calcium silicate, iii) alumino-silicate with low to moderate calcium, and iv) calcium-rich alumino-silicate. They also studied the reactivity by using synthesized glasses [38]. The work found one critical observation that the different glasses showed different levels of reactivity. Both studies [33,38] revealed that Ca-rich alumino-silicate has the fastest reactivity and silicate is the slowest.

Morphologies and chemical composition of individual fly ash particles were recently studied using the lab-scale micro-computed tomography (mCT) and SEM/EDS along with synchrotron-based nano computed tomography (nCT) and nano X-ray fluorescence (nXRF) [34,35,39]. Though several studies [34–36,40] showed that the fly ash particles investigated have multiple phases, the particles investigated are primarily composed of a single dominant phase mixed with minor phases. This is another critical observation.

By combining two critical observations obtained from the previous studies, the elemental composition of a fly ash particle can be an indication of the major phase in that particle and thus this provides an important opportunity to study the variance of these elemental compositions of individual particles and their effectiveness in a concrete mixture.

The first portion of the paper examines universal interrelationships among the elemental oxides in thousands of individual fly ash particles through a technique named automated scanning electron microscopy (ASEM) [28,41–44]. It is a powerful method because it can investigate a statistically significant number of particles without human intervention. The chemical composition of thousands of individual fly ash particles collected from the ASEM method is then analyzed using principal component analysis (PCA) to explore the universal interrelationships. After establishing an interrelationship between the chemistries of these individual particles for 20 different fly ashes, the performance of a subset of 12 of these fly ashes in concrete is investigated for their

Table 2
Properties of Type I portland cements used in the preparation of concrete.

Chemical test results (%)					
SiO2	Al2O3	MgO	Fe2O3	CaO	SO3
20.77	4.57	2.37	2.62	62.67	3.18
Na_2O	K_2O	TiO_2	P_2O_5	SrO	BaO
0.19	0.32	0.34	0.14	0.22	0.07
Phase concentration (%)					
C_3S	C_2S		C_3A		C_4AF
52.13	20.22		7.68		7.97

strength and electrical resistivity of the concrete surface [45].

This paper does not focus on the theoretical understanding of why universal interrelationships were observed. Instead, this paper aims to report the universal interrelationships of the individual particles and to make a tie between the measurements of the abundance and fly ash particle chemical composition and the subsequent performance in concrete. These findings are an important step to the improved classification of fly ash, an increase in usage of the waste material. In addition, these findings can improve the prediction of the performance in concrete, which cannot effectively be done using the previous classification based on the bulk chemistry of fly ash.

2. Materials

Twenty different fly ashes were investigated in this study. According to ASTM C618 [26], ten of the fly ashes were Class C and the other ten fly ashes were Class F. All of these fly ashes were obtained from different sources in the United States. Thus, fly ashes were produced from varying coal sources, boiler designs, and collection conditions. Elemental oxides contents for 20 fly ashes were summarized in Table 1. Table 1 shows results obtained from both using XRF as per ASTM D4326 [46]and the ASEM method as per a previous publication [28].

The analysis of the Type I ordinary portland cement (OPC) used in this study is summarized in Table 2. This cement was used to prepare all concrete mixtures in the study. Limestone and natural sands were used as a coarse aggregate and a fine aggregate. Both of them were locally available in Oklahoma. The specific gravities of coarse and fine aggregates were both 2.6 and their absorptions were, respectively, 0.64% and 0.55%.

3. Experimental methods

3.1. ASEM investigation

The ASEM method uses SEM-EDS (Aspex Explorer PSEM-EDS) with an image analysis operating system. The procedure to investigate fly ash was published elsewhere [28,39]. This method has important advantages over the conventional analysis of bulk chemistry using XRF [28,39,47,48]. The primary advantage of ASEM method is that the analysis can rapidly measure the physical and average chemical information of an individual particle and collect the information of thousands of particles in a reasonable timeframe. With current settings and equipment the method can investigate the elemental composition, size, and shape of approximately 350 particles per hour with no intervention by the user [28]. One challenge with this method is that these particles are not flat and so they violate one of the assumptions of EDS analysis. To account for this the Armstrong and Love-Scott [49,50] and Armstrong – Buseck [51,52] particle correction models were used. These models take into account the shape of the particle and make corrections to the collected k-ratios. This was done for 12 elements (Na, Mg, Al, Si, P, S, K, Ca, Ti, Fe, Sr, and Zr) by using CalcZAF [53,54]. The CalcZAF shape model best suited for a sphere was used in the analysis. It should be noted that, when the analytical compositions are normalized to 100%, the dependence of the shape is significantly decreased and the deviation of models is less than 10% [55]. Therefore, slight changes of shapes in the fly ash particles are not expected to affect the quantitative results of the ASEM method. This approach has been validated in previous publications [28].

Table 3
Summary of instrument setting, scanning setting, and EDS setting used for ASEM technique.

Instrument setting	
Spot size	40%
Accelerating voltage	~20 kV
Probe current[a]	1.15–1.20 nA
Scanning setting	
Magnification	2500×
Brightness	−15%
Contrast	90%
Working distance	17–18 mm
Aspect ratio	≤1.3
Search dwell time	16 μsec
Measure dwell time	32 μsec
Threshold lower detect[b]	128
Threshold lower measure[b]	64
EDS setting	
Minimum counts per second	3500
Live time (acquisition time)	5 s

[a] The probe current collected on a Faraday cup.
[b] Gray scale value (from 0 to 255).

Table 3 shows the summary of the instrument settings. Consistent beam energies were maintained by keeping the probe current constant by using a Faraday Cup and pico-ammeter. Table 4 shows the average values of standard deviation for three repeat measurements of 50 fly ash (Class C) particles. Additional work on the repeatability and accuracy of the ASEM method has been presented in other publications [28–30,40]. More detailed sample preparation and procedures for the ASEM method are found in Appendix A and other literature [28,39].

3.2. Principal component analysis

Principal component analysis (PCA) is a statistical method that can be used to reveal complex relationships that underlie a complex dataset. This technique uses a mathematical algorithm to reduce the dimensionality of the data while still retaining as much information as possible [56–58]. In this paper, PCA analysis was used to study the underlying relationship for 12 elemental oxides for 2000 particles from each fly ash. This number of particles was used as previous studies showed that this number of particles was enough to be a representative sample of fly ash [28]. Each fly ash data is composed of 2000 measurements and each measurement contains 12 variables. The PCA does not include diameter as a variable because the particles in fly ashes used had similar size distribution as discussed later in the paper. The particle size distribution for fly ashes used in this paper can be found in Section 4.2 and Fig. 1.

The software package R was used for this analysis [59]. A centered

Table 4
Average values of standard deviation for three independent measurements of 50 fly ash particles [29].

Element	Standard Deviation (%)
Silicon, Si	0.3
Aluminum, Al	0.4
Iron, Fe	0.7
Calcium, Ca	0.8
Magnesium, Mg	0.3
Potassium, K	0.6
Sodium, Na	0.6
Sulfur, S	0.2
Phosphorus, P	1.6
Morphology	**Standard Deviation**
Average diameter (μm)	0.1
Perimeter (μm^2)	0.4

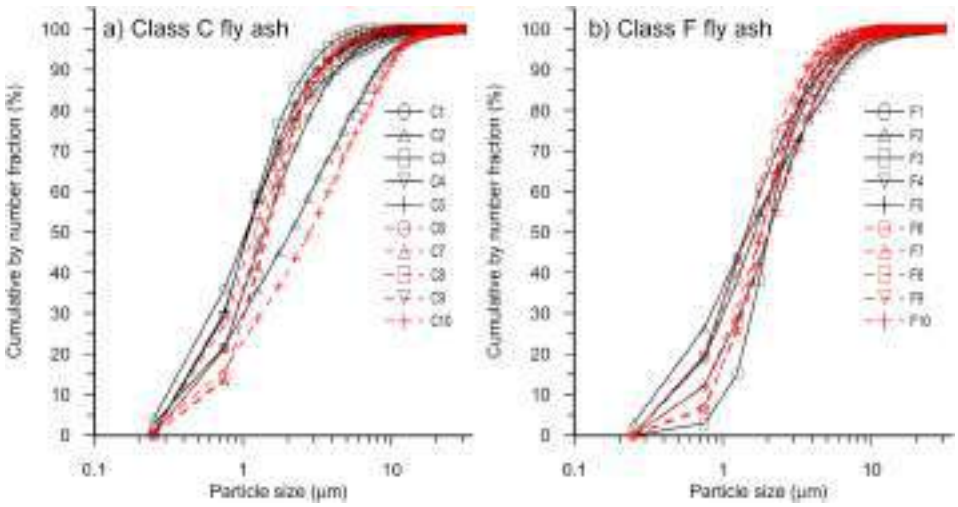

Fig. 1. Comparison of the particle size distribution by number fraction of the fly ashes investigated (0.5 μm bin size).

Table 5
Proportions of concrete mixtures.

Material	Quantity (kg/m^3)	
	Fly ash concrete	Control concrete
Cement	290	363
Fly ash[a]	72	–
Coarse aggregate	1098	1104
Fine aggregate	714	721
Water	163	163
w/cm ratio	0.45	0.45

[a] C1, C2, C3, C4, C5, C6, C7 F1, F2, F3, F4, and F5.

log-ratio (clr) transformation was used to analyze the data as it is preferred for compositional data analysis [60–63]. More details on data transformation and the discussion of the PCA method is given in Appendix B.

3.3. Concrete specimen preparation

Thirteen concrete mixtures were prepared using twelve different fly ashes (C1, C2, C3, C4, C5, C6, C7, F1, F2, F3, F4, and F5) and one control mixture without fly ash. These fly ashes were chosen as they covered a wide range of different chemical compositions. The mixture proportions (kg/m^3) are given in Table 5. All concrete mixtures used the same w/cm of 0.45. The mixtures with fly ash were used at a 20% replacement by mass of cement. No chemical admixtures were included to reduce the number of variables in the study.

Aggregates were prepared and stored in a temperature-controlled room (22 °C) at least 24 h before mixing. Their batch weights were corrected for the moisture content of aggregates. The aggregates were charged into the mixer along with approximately two-thirds of the mixing water. This was mixed for 3 min. Next, any clumped fine aggregate was removed from the walls of the mixer. Then the cement and fly ash were loaded into the mixer, followed by the remaining mixing water. The mixer was turned on for three minutes. Once this mixing period was complete, the mixture was left to "rest" for the following two minutes while the buildup of material along the walls was removed. Cylinder samples (10.2 cm × 20.3 cm) were prepared, covered, and initially cured for 24 h. After this initial curing, cylinder samples were demolded and stored in the moisture room at 23 °C for specific periods. Compressive strength testing was conducted at 3, 7, 14, 28, 56, 90, and 180 days in accordance with ASTM C39 [64] and the surface resistivity (AASHTO T34 [45]) was also measured at the same days.

3.4. Linear model development

These concrete specimens were prepared to explore the potential application of the particle data. As one potential application, the compressive strength and the electrical resistivity were correlated to the particle data using two linear models. These linear models for compressive strength and electrical resistivity were validated using the three-fold cross-validation. In this validation 2/3 of the results are used to train a model and then this is validated with the remaining 1/3 of the data. This process is repeated 100 times by randomly sampling 2/3 of the experimental data and the variation of the results are compared. More details of the validation process are summarized in Appendix C.

4. Results of ASEM and PCA

4.1. Bulk chemical compositions of fly ashes

Table 1 shows the bulk chemical composition obtained by both XRF and ASEM for all twenty fly ashes. The elemental oxide contents obtained from ASEM for all 20 fly ashes were very close to the corresponding contents obtained from XRF. 12 out of 193 or 6% of comparisons showed more than an absolute difference of 5%. This indicates that the two methods agree well with one another. C5 and F3 showed 10.1% and 11.1% difference for SiO_2 and 8% and 5.3% for CaO between XRF and ASEM method, respectively. In terms of Na_2O, C6 and C10 showed 3.4% and 3.0% difference between the two methods. This seems to mainly result from the sampling process for either ASEM method or XRF because the consistency and accuracy of ASEM methods have been confirmed in the previous work [28,29]. It should be noted that these differences in bulk chemistry should not affect the PCA results because the chemical information of each particle is a critical factor in PCA analysis. In addition, the relationships were derived from the compositional relationship from 20 different fly ashes with 2000 particles and 12 different oxides for each fly ash, which is a robust number of observations.

4.2. Particle size distribution

In addition to the composition, the ASEM technique measures the size of the particle and produces a particle size distribution (PSD). Previous research by Aichele et al. [65] analyzed PSDs of a glass bead, fly ashes, and soft latex particles using both ASEM and acoustic attenuation spectroscopy. This work reported that both analysis methods provided similar PSD despite the intrinsically different physics in both techniques [65]. The cumulative PSDs of 20 fly ashes investigated are

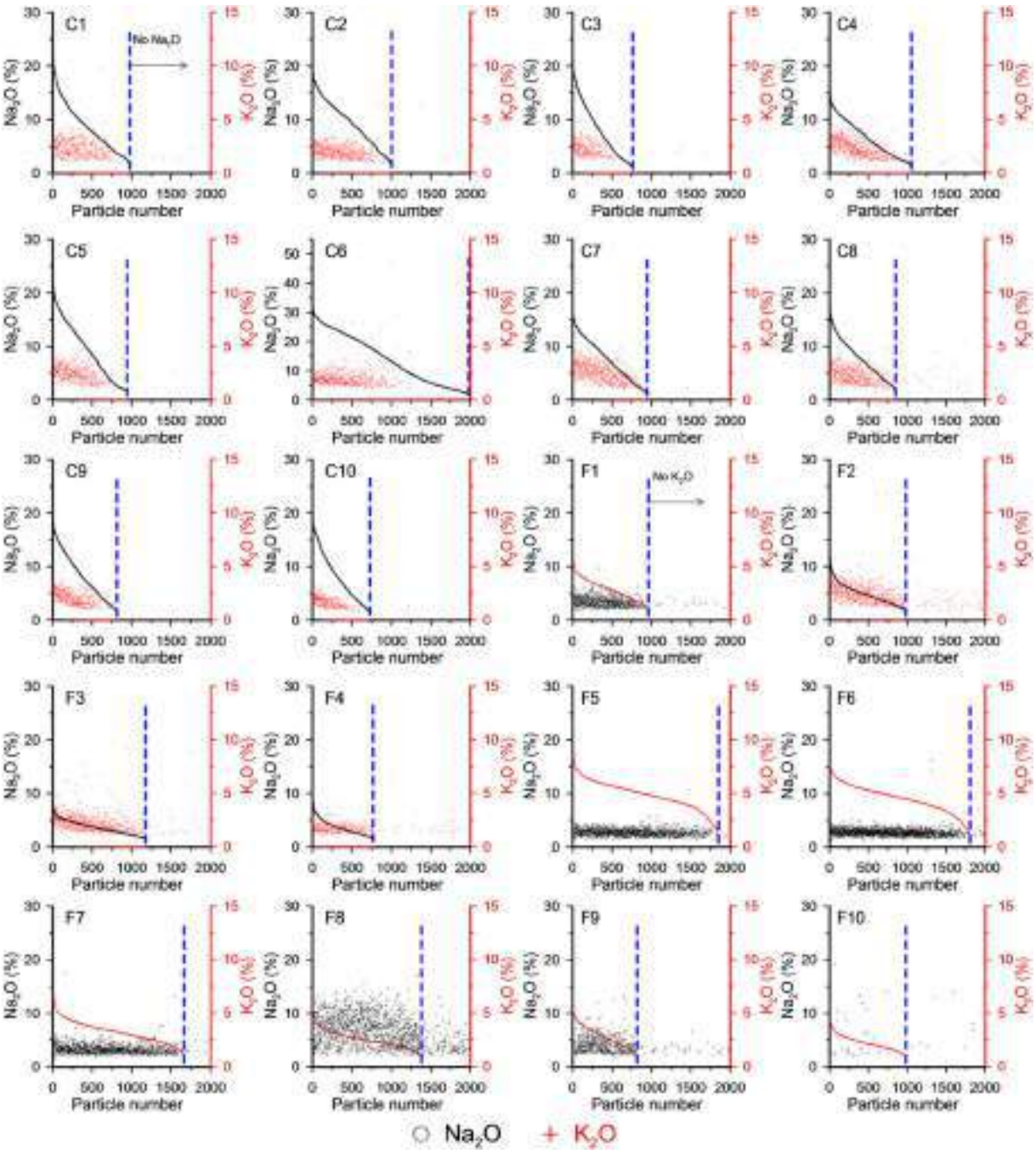

Fig. 2. A similar correlation between Na_2O and K_2O in 20 fly ashes. Each plot is rearranged in decreasing amount of either Na_2O or K_2O (whichever has the higher number of particles). The plots show that Na_2O co-exists with K_2O in individual particles (the left side of the blue dashed line). (For interpretation of the references to color in this figure legend, the reader is referred to the Web version of this article.)

summarized in Fig. 1. Most fly ashes varied in size between 0.2 μm and 50 μm and showed a quite narrow range of PSDs. Class C fly ashes showed a slightly wider range of PSDs than Class F fly ashes. Since PSDs from 20 fly ashes are similar to each other as shown in Fig. 1, PCA analysis performed using the elemental compositions of particles.

4.3. PCA results

As mentioned previously, each fly ash obtained from the ASEM method was composed of chemical compositions of 2000 particles and each particle contained 12 compositional elemental oxide contents by mass. In other words, total fly ash data was composed of 40,000 measurements and each measurement contains 12 variables. To deal with this large data, PCA was performed in this study.

The variance of the data explained by the first ten principal components (PCs) is summarized in Table A1. More details about the variance of data can be found in Appendix B. In summary, the analysis of PC1 and PC2 has the potential to provide important insights into the relationships of the underlying chemical composition of the fly ash particles. Therefore, the analysis of using PC1 and PC2 was used in this work.

To visualize the results of the PCA, the data was presented with a loading plot. A loading plot is a vector-based plot where each vector starts at the origin (see Fig. A1). This loading plot can be used to

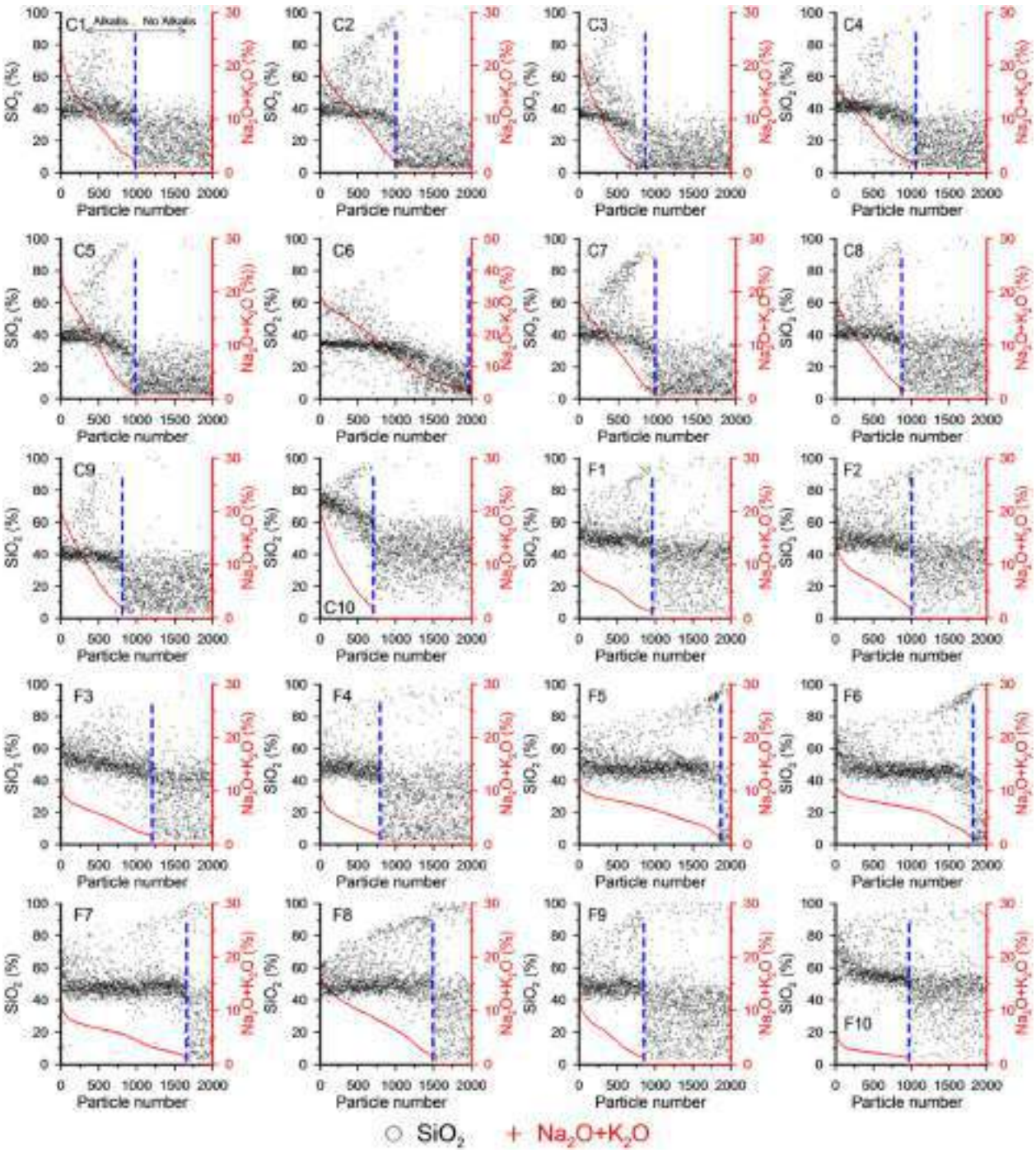

Fig. 3. A similar correlation between SiO_2 and $Na_2O + K_2O$ in 20 fly ashes. Each plot is rearranged in a decreasing amount of [$Na_2O + K_2O$]. The plots show that particles containing [$Na_2O + K_2O$] are associated with the higher content of SiO_2 (more than 35%) as shown in the left side of the blue dashed line. (For interpretation of the references to color in this figure legend, the reader is referred to the Web version of this article.)

qualitatively interpret the interrelationships of the chemical composition within individual fly ash particles [57,58,66,67]. The loading plot provides the underlying correlation among elemental oxides: i) elemental oxides tending to co-exist in a particle (similar correlation), and ii) elemental oxides tending to exclude each other (inverse correlation). Full details about the analysis of loading plots obtained from 20 fly ashes can be found in Appendix B. In this section, the important and interesting findings from PCA are summarized below:

- All 20 fly ashes show consistent trends of chemical composition regardless of their sources.
- Na_2O and K_2O, SiO_2 and [$Na_2O + K_2O$], and CaO and MgO, SO_3 and P_2O_5 show a similar correlation to one another within individual particles.
- CaO and [$Na_2O + K_2O$], [$Na_2O + K_2O$] and [SO_3 and P_2O_5] were found to inversely correlate to one another within the individual particles.

These qualitative observations obtained from PCA loading plots are interesting because it suggested universal trends regardless of fly ash sources. These trends would be very challenging to manually find by investigating the 480,000 combinations investigated in this work (20 fly

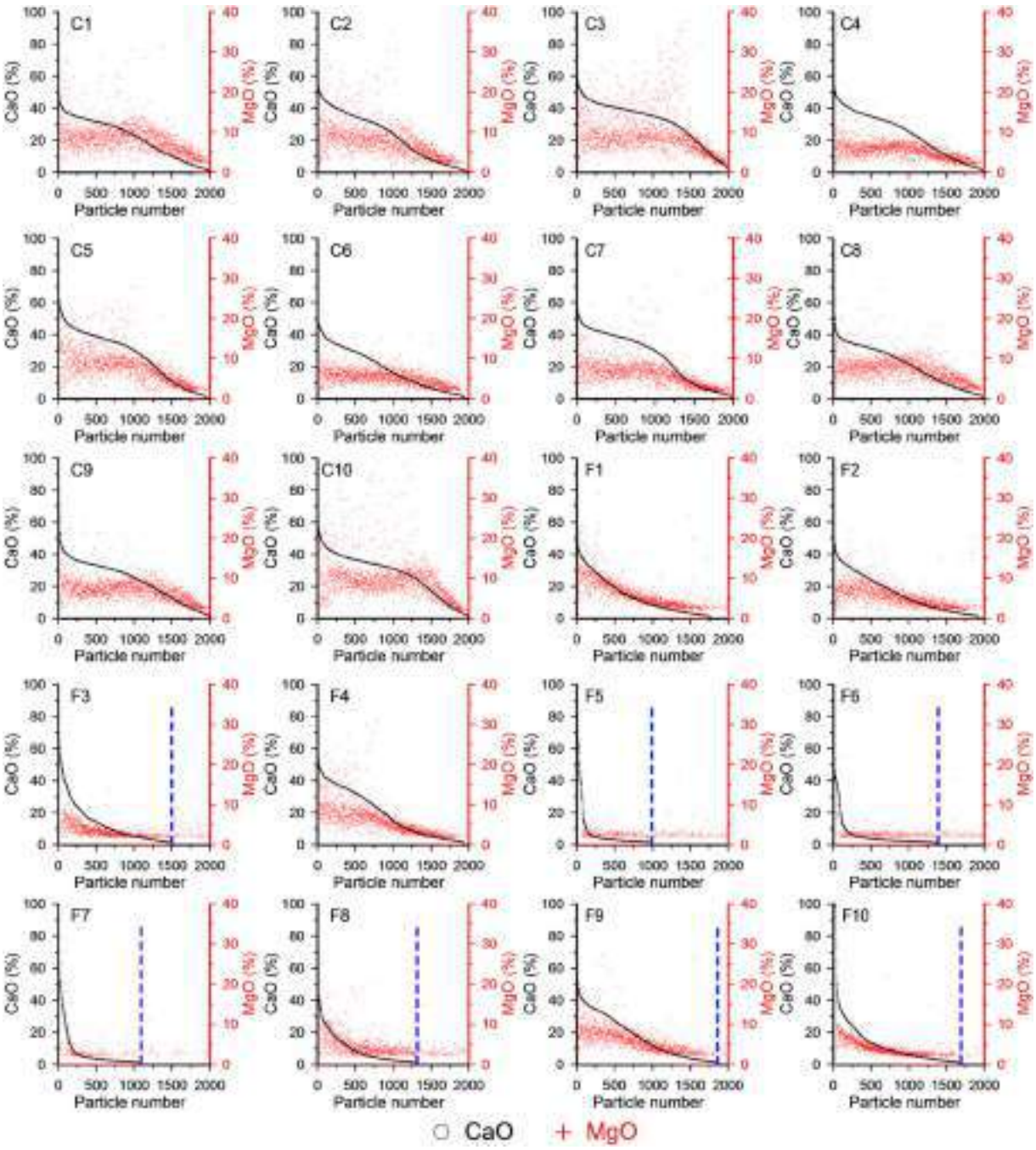

Fig. 4. A similar correlation between CaO and MgO in 20 fly ashes. Each plot is rearranged in a decreasing amount of CaO. The plots show a strong correlation between the CaO and MgO.

ashes × 2000 particles per fly ash × 12 compounds). However, these interrelationships have not been verified and thus work will be done to confirm these predictions with quantitative comparisons.

4.4. Verification of interrelationships among elemental oxides

To investigate the trends suggested by PCA, comparisons are made of the relationship of individual oxides to further investigate the trends suggested by the loading plots. Fig. 2 through 7 examine the chemistry of 2000 particles per fly ash. The plots have two different Y-axes to compare different oxides in the same particle and the X-axis is the particle number.

4.4.1. Na_2O vs. K_2O

Both Na_2O and K_2O were suggested to play an important role in both similar and inverse correlations among elemental oxides, particularly SiO_2 and CaO. Fig. 2 shows the correlation between Na_2O and K_2O for all 20 of the ashes investigated. Each plot in Fig. 2 was rearranged in a decreasing amount of either Na_2O or K_2O (whichever has a higher number of particles). For example, C3 fly ash, 737 out of 2000 particles contained Na_2O and 326 out of 2000 particles had the K_2O. Therefore, the particles were arranged in terms of the contents of Na_2O when correlating K_2O with Na_2O (see C3 plot in Fig. 2). A blue dashed line is used to show where the particles with either Na_2O or K_2O are no longer detectable. The results show that for the majority of the particles when Na_2O was observed then K_2O was also found. For example, 99% particles

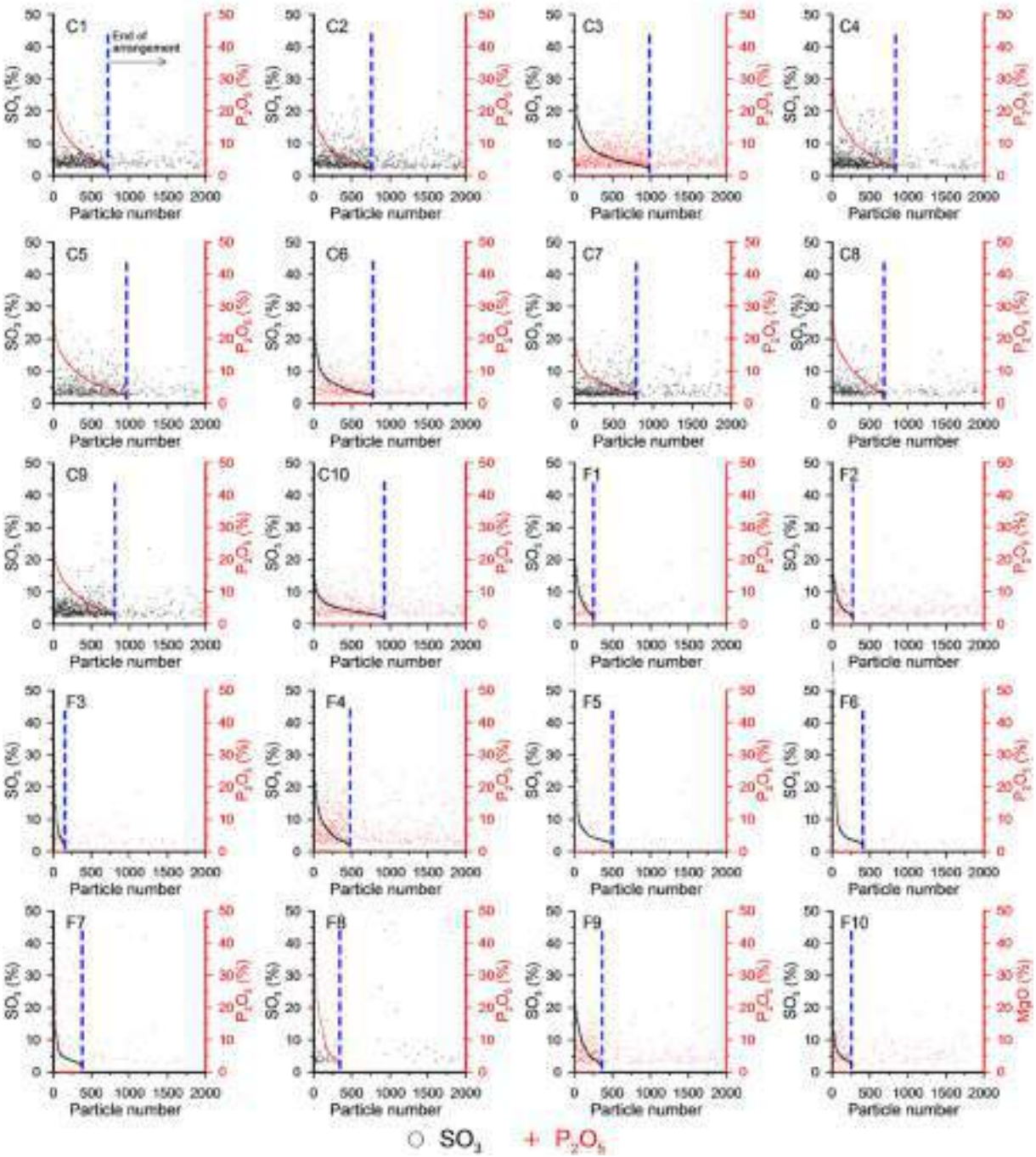

Fig. 5. A similar correlation between SO_3 and P_2O_5 in 20 fly ashes. Each plot is rearranged in decreasing amount of either SO_3 or P_2O_5 (whichever has the higher number of particles). The plots show that SO_3 tend to co-exist with P_2O_5 in individual particles (the left side of the blue dashed line). (For interpretation of the references to color in this figure legend, the reader is referred to the Web version of this article.)

(323 out of 326 particles) containing K_2O in C3 fly ash also contain the Na_2O as shown in Fig. 2. This confirms the finding from the PCA loading plot.

There are particles that contain only Na_2O or K_2O and not the other oxide. For example, fly ash C3 had 737 particles with Na_2O and 326 with K_2O and thus there must be some particles that only contain Na_2O. However, the correlation suggested by the PCA still holds because the majority of the K_2O containing particles co-exist with Na_2O (323 particles) as shown in Fig. 2.

Since both Na_2O and K_2O show a similar correlation, the remainder of the analysis will just look at the sum of these oxides or the $Na_2O + K_2O$. This combined group of particles was then compared with the other elemental oxides to verify the correlation obtained from the analysis of the loading plots.

4.4.2. *SiO_2 vs $[Na_2O + K_2O]$*

Another correlation that was suggested by the PCA analysis was SiO_2 and $[Na_2O + K_2O]$. Plots comparing these data sets are shown in Fig. 3. The $[Na_2O + K_2O]$ data has been plotted from high to low values. The data show that particles with relatively high contents of SiO_2 (more than 35%) were observed in the particles containing alkalis (the left region of the blue dashed line in Fig. 3). However, particles without alkalis had

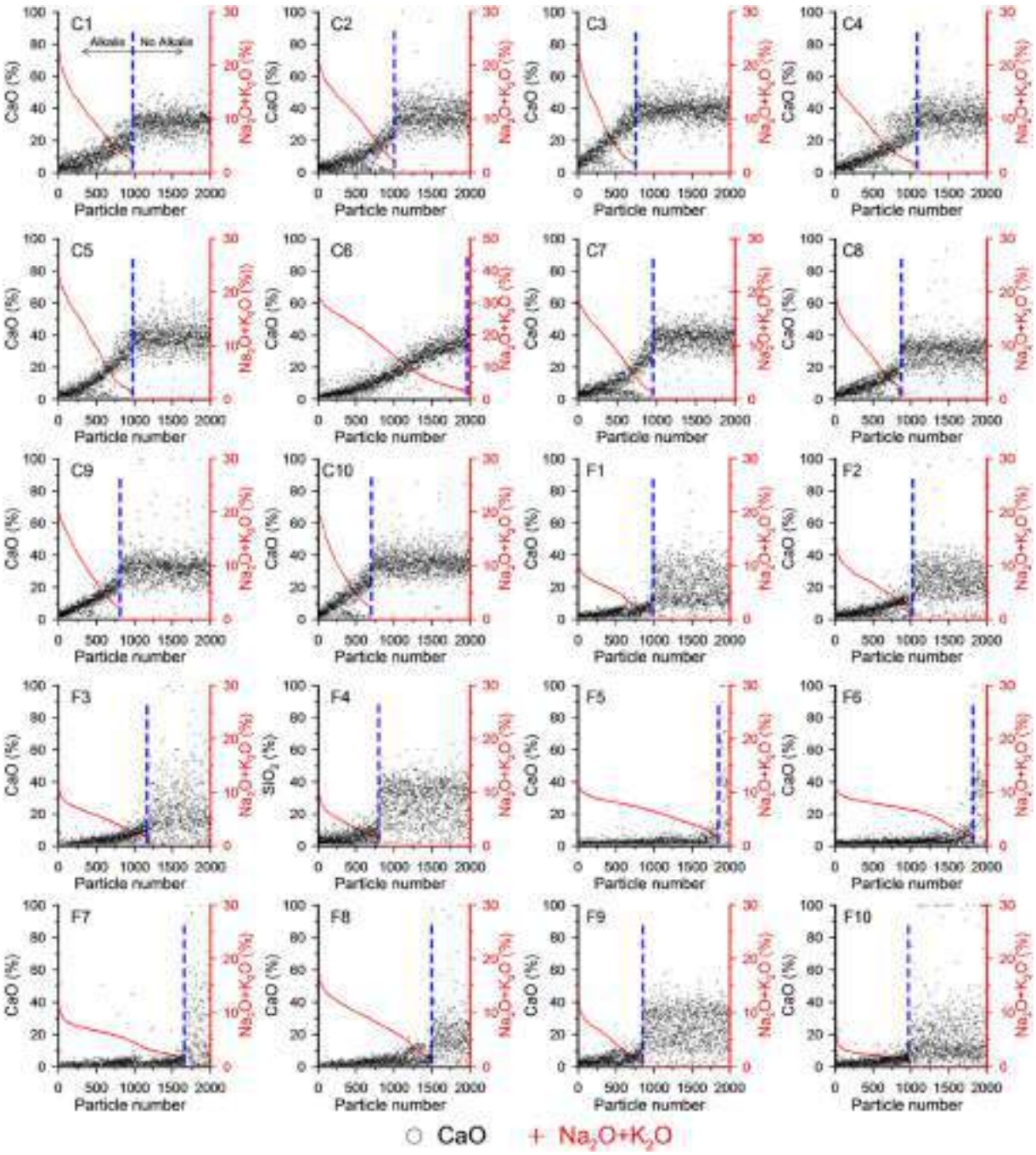

Fig. 6. Opposite correlation between CaO and [$Na_2O + K_2O$] in 20 fly ashes. Each plot is rearranged in a decreasing amount of [$Na_2O + K_2O$]. CaO content increases as a decrease in [$Na_2O + K_2O$] content (the left side of blue dashed line). The particles without [$Na_2O + K_2O$] generally have increase content of CaO (the right side of blue dashed line). (For interpretation of the references to color in this figure legend, the reader is referred to the Web version of this article.)

lower amounts of SiO_2 as shown in the right region of the blue dashed line in Fig. 3. This trend was consistently observed from all 20 fly ashes except for C6. This fly ash had a bulk alkali content of 13.4%, respectively. Therefore, this has either Na_2O or K_2O present in almost all of the observed particles.

4.4.3. *CaO vs MgO*

The PCA analysis showed a strong correlation between the CaO and MgO and this can be seen in Fig. 4. For most of the fly ashes investigated it was observed that the contents of CaO and MgO decreased together in particles. Such a similar relation is not clearly observed in the F4, F6, F7, and F8 due to the small amount of CaO (see Table 1). However, even in these fly ashes, it is common for both CaO and MgO to be present together. The red crossed particles (particles containing MgO) on the left side of the blue dashed line were clearly occurred more often than those on the right side of the blue dashed line. This again reinforces the findings from PCA.

4.4.4. *SO_3 vs P_2O_5*

Plots showing the correlation between SO_3 and P_2O_5 are shown in Fig. 5. The oxide which had a higher number of particles is rearranged from the highest content in the same way for the correlation between K_2O and Na_2O. Though the trend is not as strong as Na_2O and K_2O, these plots clearly show that when SO_3 is present then so is P_2O_5. The analysis

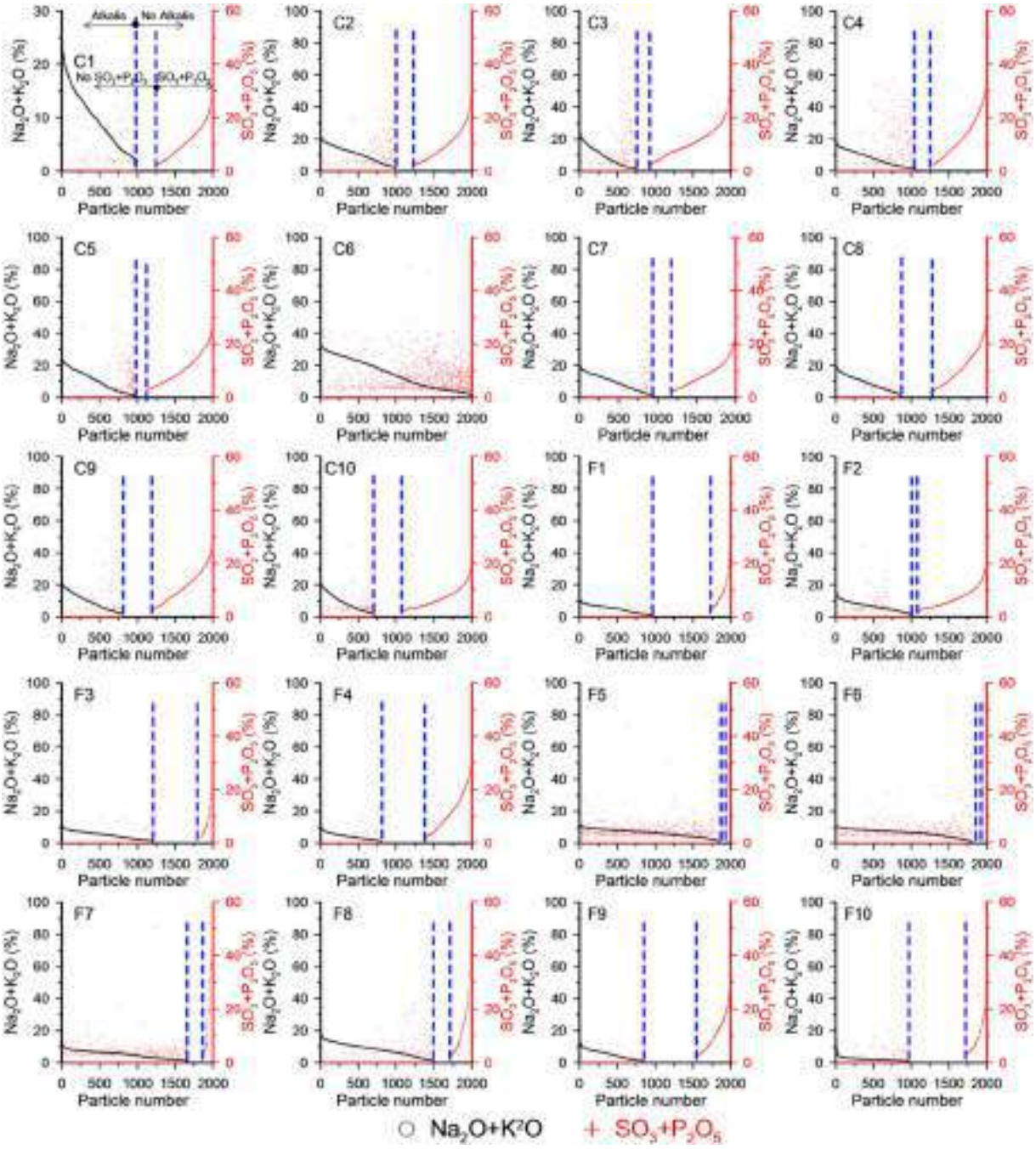

Fig. 7. Opposite correlation between $Na_2O + K_2O$ and $P_2O_5+SO_3$ in 20 fly ashes. Each plot is rearranged in decreasing amount of $[Na_2O + K_2O]$ and $[SO_3 + P_2O_5]$. The plots show clear four groups. a) Group A: $Na_2O + K_2O > 0$ and $SO_3 + P_2O_5 = 0$ (left side of the left blue dashed line), b) Group SP: $K_2O + Na_2O = 0$ and $SO_3 + P_2O_5 > 0$ (right side of the right blue dashed line), c) Group NASP: $Na_2O + K_2O = 0$ and $SO_3 + P_2O_5 = 0$ (between blue lines), and d) Group ASP: $Na_2O + K_2O > 0$ and $SO_3 + P_2O_5 > 0$ (floating red crosses). (For interpretation of the references to color in this figure legend, the reader is referred to the Web version of this article.)

also shows that there are particles that only contain P_2O_5 and no SO_3.

4.4.5. *CaO vs $[Na_2O + K_2O]$*

An inverse correlation between $[Na_2O + K_2O]$ and CaO was predicted by the PCA loading plots (see Fig. A2) and Fig. 6 confirms this. For each fly ash, the chemical compositional data of particles were rearranged in terms of the content of $[Na_2O + K_2O]$ and an inverse correlation was observed for all 20 fly ashes. The data points on the left of the dashed lines in Fig. 6 show that the CaO content increases as a decrease in $[Na_2O + K_2O]$ content. The particles without alkalis are located to the right of the dashed line. Those particles generally had increased CaO content. With decreasing alkali contents, the CaO increased up to around 30%–40%. Only a few particles with a CaO content above 30% were found to have either Na_2O or K_2O. This trend holds for all of the fly ashes. Fly ash C6 had Na_2O or K_2O in almost every particle investigated. However, in this fly ash, the inverse correlation between $[Na_2O + K_2O]$ and CaO can be still observed.

4.4.6. *$[Na_2O + K_2O]$ vs.$[SO_3 + P_2O_5]$*

These oxides ($[Na_2O + K_2O]$ vs. $[SO_3 + P_2O_5]$) are suggested to have an inverse correlation by the PCA analysis. As shown in Fig. 7, this is largely true. The particles have been arranged by low to high amounts of $[SO_3+P_2O_5]$. The data was then arranged from high to low alkali content. This was used to show the correlation between these two variables.

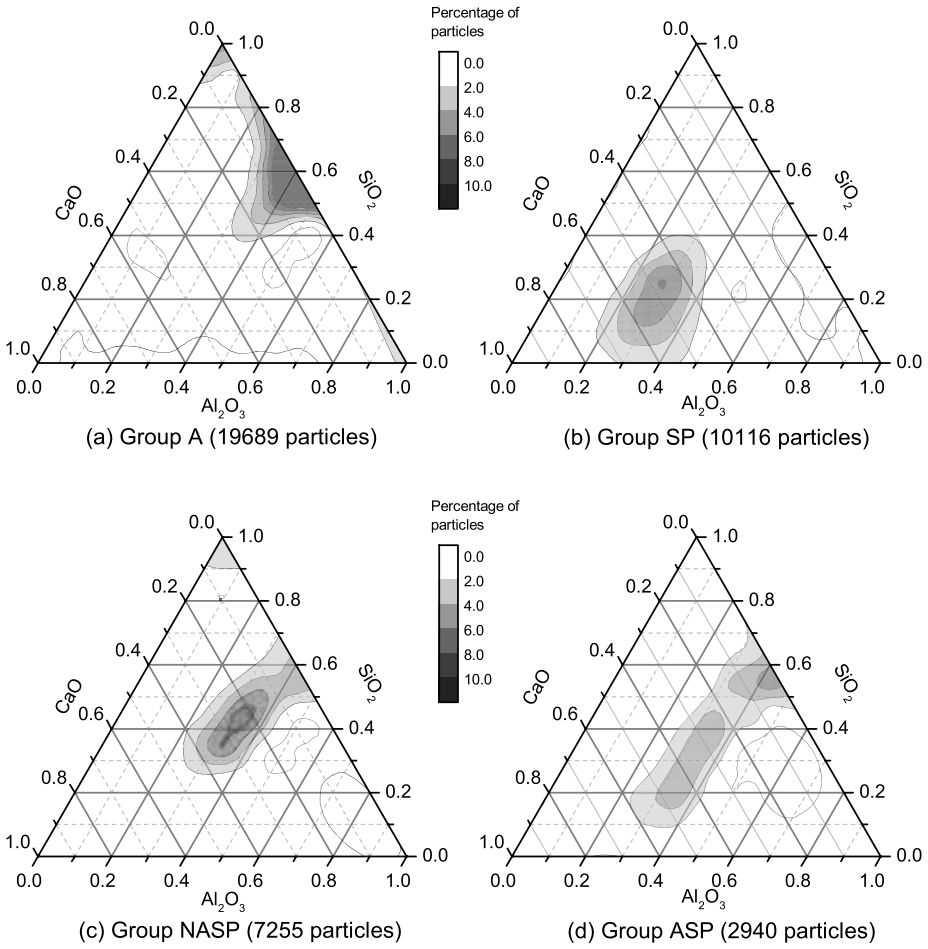

Fig. 8. Ternary density diagrams for each group obtained from 20 fly ashes. Particles are categorized in four groups with limited chemical compositions. Group ASP contains particles that are not explained by PCA results and the amount of this is very low (~7%).

For the majority of the particles, when Na_2O or K_2O were present in the particles, there was no P_2O_5 or SO_3 (these are on the left side of the blue dashed line). This trend indicates that the particles containing the K_2O or Na_2O somehow tend to exclude the content of [P_2O_5 + SO_3]. This trend is observed for all of the fly ashes investigated except C6. In this fly ash, K_2O and Na_2O were present in almost all of the particles. Also, for several of the fly ashes, there were particles that did not contain Na_2O, K_2O, P_2O_5, or SO_3. These particles are between the dashed lines in Fig. 7.

5. Application of particle data

5.1. Grouping particles using the interrelationships among elemental oxides

The individual particle data allow for exploring numerous ways to categorize the particles into different groups based on their elemental compositions. The previous section clearly showed that fly ash particles have consistent trends among the different elemental oxides regardless of their sources. In this study, the authors suggest one possible grouping scheme based on these consistent trends described in section 4.4.1 to 4.4.6 in order to explore the usefulness of this data. Many of the predicted relationships with PCA used either [K_2O + Na_2O] or [SO_3 + P_2O_5]. In fact, these groups were found to vary inversely as shown in Fig. 7. Alkali contents seem to be associated with contents of CaO and SiO_2 as described in sections 4.4.2 and 4.4.5. Therefore, any fly ash particle can be grouped by one of the following four classifications: (a) Group A (alkalis): $Na_2O + K_2O > 0$ and $SO_3 + P_2O_5 = 0$, (b) Group SP (sulfur and phosphorous): $K_2O + Na_2O = 0$ and $SO_3 + P_2O_5 > 0$, (c) Group NASP (no alkalis, sulfur, or phosphorous): $Na_2O + K_2O = 0$ and $SO_3 + P_2O_5 = 0$, (d) Group ASP (alkalis, sulfur, and phosphorous): $Na_2O + K_2O > 0$ and $SO_3 + P_2O_5 > 0$. Group ASP contains particles that are not explained by PCA results and the amount of particles in this group is very low (~7%).

To examine the chemical composition of these particles ternary density diagrams were made for each of these four groups and are shown in Fig. 8. Each of the 40,000 fly ash particles investigated for this paper is represented in the plot. Due to the primary interest of Si–Al–Ca system, the weight % of SiO_2, Al_2O_3, and CaO are normalized to 100% for the ternary density plot. Fig. 8 (a) showed the density plot of 19,689 particles in Group A that contains K_2O or Na_2O without SO_3 and P_2O_5. The SiO_2 was found to be between 50% and 70%, CaO less than 20%, and Al_2O_3 between 30% and 50%. However, as shown in Fig. 8 (b), the 10,116 particles in Group SP have decidedly different chemistry (SiO_2 weight between 10% and 30%, CaO weight between 35% and 60%, and Al_2O_3 weight between 25% and 40%). Group NASP and Group ASP showed in Figs. 8 (c) and (d) have chemical compositions between Group A and Group SP. It should be noted that the fraction of Group ASP in fly ash was generally quite low (less than 10%). 1262 out of 2940 particles in Group ASP just came from 2 fly ashes (C6 and F5). These two fly ashes had alkali oxides much greater than the other fly ashes. Therefore, the majority of the particles fell into either Group A or Group ASP, For C6 and F5 fly ashes, this Group ASP might be important for their performance in concrete.

Since these groups describe every particle found within the fly ash investigated, different percentages of these particles may be able to be used to characterize a bulk fly ash sample. A summary of this classification for all of the fly ashes investigated is given in Table 6. Class C fly ashes generally have greater CaO contents than Class F fly ashes. In this

Table 6
Four different groups, their properties, and fractions of groups in fly ashes.

Property	Group A	Group SP	Group NASP	Group ASP
$Na_2O + K_2O$	>0	0	0	>0
$SO_3 + P_2O_5$	0	>0	0	>0
SiO_2	50–70%	10–30%	30–50%	20–60%
CaO	<20%	35–60%	15–35%	5–50%
Al_2O_3	30–50%	25–40%	25–35%	25–45%
Fly ash	**Percentage by number of particles (%)**[a]			
	Group A	**Group SP**	**Group NASP**	**Group ASP**
C1	45	36	15	3
C2	43	38	12	7
C3	31	54	9	6
C4	44	35	12	9
C5	42	45	8	5
C6	58	0	0	42
C7	44	41	12	3
C8	41	39	17	2
C9	37	41	19	3
C10	31	46	18	4
F1	48	14	38	1
F2	49	16	33	2
F3	59	8	32	1
F4	39	30	30	1
F5	71	4	4	21
F6	74	4	6	16
F7	71	7	9	12
F8	70	14	12	5
F9	42	22	36	1
F10	47	14	37	2

[a] 2000 particles were analyzed for each fly ash.

classification, Class C fly ashes except for C6 generally have a higher fraction in this Group SP [particles with a high CaO content as shown in Fig. 8(b)] than the Class F ashes. On the other hand, higher amounts of particles in Group A and Group NASP were observed from Class F fly ashes. It should be noted that Group A has the highest content of SiO_2 and the lowest content of CaO among the four groups.

Next, the contents of the bulk major oxides in each of the particle groups are shown in Fig. 9. The stacked bars show the major oxides in each of the groups and, by placing each of the fly ashes next to one another, it is easy to compare them. The variability in Group SP and Group NASP is much greater than that observed in Group A and SP. The contents of CaO and SiO_2 in Group SP varied in the range from 8.3% to 55% and from 11.6% to 49.6%, respectively. These wide variations of Group NASP and Group ASP can also be seen in the wide distribution of the ternary plot shown in Fig. 8(c) and (d). However, Group A and Group SP from different fly ashes showed similar chemical compositions. This chemical composition consistency of Group A and Group SP will be discussed in Section 6.

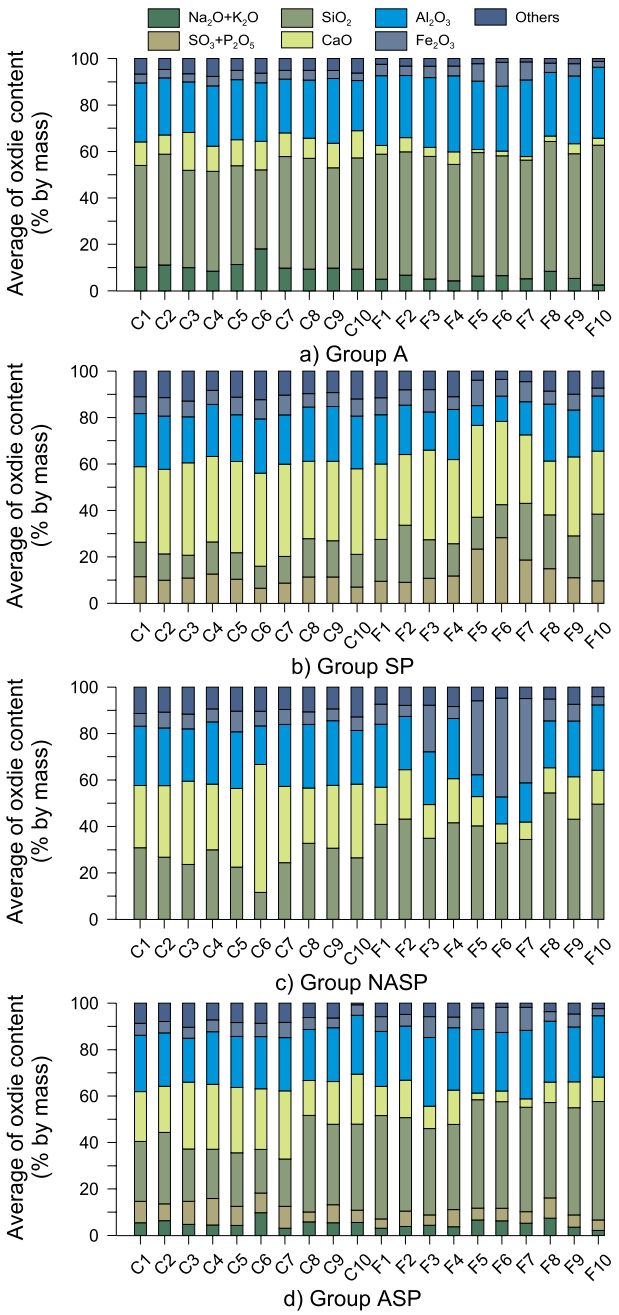

Fig. 9. Chemical composition of each group from 20 fly ashes.

5.2. Relation between the fraction of groups and compressive strength of concrete

To explore the usefulness of this grouping scheme, a simple linear model was derived. It should be noted that the goal of this linear model is not to provide a comprehensive and rigorous model to predict the compressive strength but to show the benefit of the individual particle data of fly ash. The fraction of Group ASP was not included in the linear model because the sum of the four groups must be 100%. Therefore, if one knows three other groups, the final group (Group ASP) is determined.

$$\text{Compressive Strength} = \beta_{s1}\cdot G_A + \beta_{s2}\cdot G_{SP} + \beta_{s3}\cdot G_{NASP} + \beta_{s4}\cdot \ln(t_{days}) \quad (1)$$

where G_A, G_{SP}, and G_{NASP} are, respectively, the fraction (%) of Group A, Group SP, and Group NASP for given fly ash, t_{days} is the time (>0). The corresponding linear coefficients are, respectively, β_{s1}, β_{s2}, β_{s3}, and β_{s4}. To simplify the strength development over time, the effects of fly ash groups on the strength development were assumed to be independent on time and a logarithmic function of time was used in Eq. (1). In addition, the effect of PSD on each group was not considered in this linear model because all four Groups show similar cumulative PSDs as shown in Fig. 10. The results of the modeling are summarized in Table 7 and Fig. 11.

As shown in Fig. 11, the linear model accurately explained the compressive strengths of concrete samples prepared using 12 different mixtures with an R^2 value of 0.96. p values in Table 7 indicate the statistical significance of each predictor. p values for Group A, Group SP, and $\ln(t_{days})$ shown in Table 7 are very close to zero, which means that these parameters are meaningful to this model. However, the estimated coefficient (β_{s3}) for Group NASP was 0.05 and its p-value was 0.8, which indicates that Group NASP was not highly associated with the strength development.

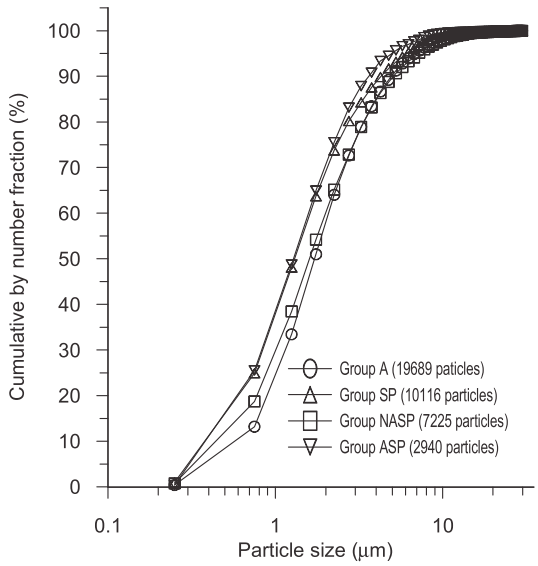

Fig. 10. Comparison of the particle size distribution by number fraction of four different groups (0.5 μm bin size).

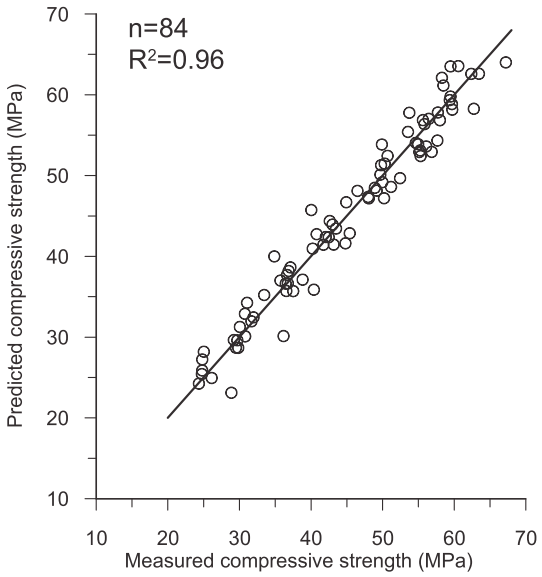

Fig. 11. Comparison of Measured compressive strength with predicted compressive strength using a linear model with 12 fly ash concretes.

5.3. Relation between the fraction of groups and electrical resistivity of concrete

The electrical resistivity of concrete is affected by the various factors, including connectivity of pores, porosity, the conductivity of pore solution, moisture content, temperature and so on [68]. Despite a large number of variables being combined into a single measurement it is still useful to understand how different particles impact the change in resistivity over time.

As shown in Fig. 12, the electrical resistivity over time is proportional to the square root of time, the water absorption equation in ASTM C1585 [69]was selected as a model equation. The general form can be shown as:

$$\text{Resistivity} = S(G_A, G_{SP}, G_{NASP}) \times \sqrt{t_{days}} = (\beta_{r1} \cdot G_A + \beta_{r2} \cdot G_{SP} + \beta_{r3} \cdot G_{NASP}) \times \sqrt{t_{days}} \quad \text{Eq. (2)}$$

, where $S(G_A, G_{SP}, G_{NASP})$ is a slope of a linear equation between resistivity and $\sqrt{t_{days}}$. This slope was expressed using a simple linear model in which the corresponding linear coefficients are, respectively, β_{r1}, β_{r2}, and β_{r3} as shown in Eq. (2). Because the electrical resistivity of fresh concrete is $<$ 0.06 kΩ m [70,71], the intercept of this equation is assumed to be zero. The results are summarized in Table 7 and Fig. 13.

The model developed using all 12 concrete mixtures explained the electrical resistivity values with an R^2 value of 0.94. The standard errors shown in Table 7 are quite small. p values indicate that Groups A and NASP are statistically meaningful but Group SP does not. It is interesting to note that Group SP used in the strength model was meaningful but it was not useful in the resistivity. This might imply that certain groups preferentially impact a specific performance of concrete.

It should be noted that the developed models used all experimental data (84 experimental compressive strengths and 84 surface resistivity data) to estimate the best-fitted parameters. Thus, this high values of R^2 in both models are generally expected because all experimental data used for the linear regression were applied for the prediction again. To validate this model, three-fold validation was applied. More details of the validation results and statistical interpretation are summarized in Appendix C. After 100 repetition of three-fold cross-validation, 100 sets of validation results could be obtained. The three-fold validation compared those 100 sets obtained from randomly selecting both training

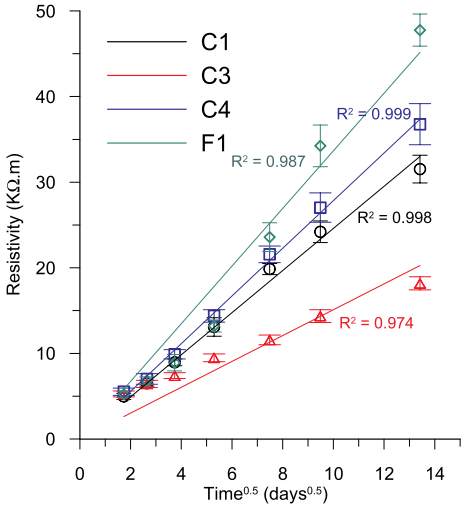

Fig. 12. A linear relation between electrical resistivity and the square root of time for C1, C3, C4, and F1 fly ash concretes.

Table 7
Model results and statistical results for resistivity of concretes.

Variables	Coeff.	Model for compressive strength				Model for electrical resistivity			
		Estimate	Std. Error	t-stat	P value	Estimate	Std. Error	t-stat	P value
Group A	β_{s1}, β_{r1}	0.242	0.013	18.184	3.8×10^{-30}	0.045	0.002	26.692	6.8×10^{-42}
Group SP	β_{s2}, β_{r2}	0.240	0.013	18.376	1.9×10^{-30}	0.000	0.002	−0.150	8.3×10^{-1}
Group NASP	β_{s3}, β_{r3}	0.005	0.020	0.241	8.1×10^{-1}	0.032	0.003	9.275	2.3×10^{-14}
$\ln(t_{days})$	β_{s4}	8.282	0.189	43.823	1.1×10^{-57}	–	–	–	–

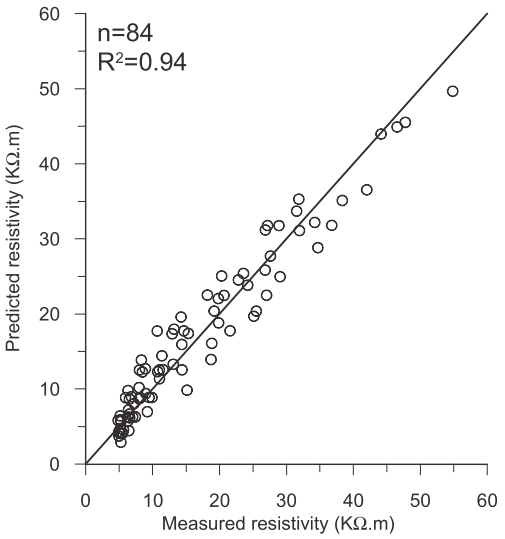

Fig. 13. Comparison of measured resistivity with predicted resistivity using a linear model with 12 fly ash concretes.

dataset (2.3 of dataset) and validation dataset (1/3 of dataset). The standard deviation of the R^2 values for two models for the compressive strength and the electrical resistivity was 0.004 and 0.001, respectively. These small variations of standard deviations for R^2 values from two models indicated the stability and robustness of these models. Therefore, these models might be used for the other datasets generated from the same mixture design with different fly ash. However, it should be noted that these models may not be applicable other mixtures with different w/c, different replacement ratios, and different cement types.

6. Discussion

The correlations predicted by PCA have been confirmed by comparing the chemistry of the individual particles. There seems to be a fundamental underlying pattern among the elemental oxides that exist for the 20 fly ashes studied in this paper. This means that there are particles with similar chemistries contained in each of the fly ashes despite being produced at different locations and with different bulk chemical compositions. Furthermore, this grouping scheme can be used to predict the effect of different fly ashes on the compressive strength and the electrical resistivity of concrete.

Though this study does not aim to build a comprehensive understanding of interrelationships among oxides, the previous literature [72–76] suggests that some of the observed interrelationships among oxides seem to be the result of the original mineral forms in pulverized coal particles. The compositions of fly ash particles are significantly influenced by inorganic substances in raw pulverized coal and the ash formation during the combustion process [72,74–76]. Inorganic substances exist as either mineral forms or non-mineral inorganic constituents in coal [72,76].

Alkali bearing minerals in coals are generally composed of illite [$K_{1.5}Al_4(Si_{6.5}Al_{1.5})O_{20}(OH)_4$], smectite [$Na_{0.33}(Al_{1.67}Mg_{0.33})Si_4O_{10}(OH_2)$] and feldspar ($KAlSi_3O_8$, $NaAlSi_3O_8$). These minerals contain both alkalis and silica but do not have calcium. Thus, these minerals might be converted to the fly ash particles in Group A, since these fly ash particles do not have calcium. Calcium in pulverized coal particles is mainly found in particles containing carbonates, including calcite ($CaCO_3$) and dolomite [$CaMg(CO_3)_2$] [73]. This might explain why CaO and MgO were found to co-exist within fly ash particles. Others have shown that Ca and Mg can further interact with aluminosilicates to form glassy phases [72].

The interrelationships highlighted in this work give a strong insight into new levels of understanding and possible classification of fly ash particles. Though the current work did not reveal the glassy phases in individual particles, this idea is similar to work by others that found repetition in the glasses found within polished sections of fly ash [33,38]. It should be noted that this work has investigated 20 different fly ashes to show that these correlations hold over a wide range of materials.

7. Conclusions

The large volume replacement of portland cement with SCMs is a promising approach to reduce the environmental impact induced by concrete; however, it is still limited due to lack of understanding of the compositional complexity of SCMs. This paper provides a potential fly ash classification technique that uses universal interrelationship among the chemical composition found by using an advanced particle analysis technique named ASEM and principal component analysis (PCA). These methods were used to investigate 40,000 fly ash particles from 20 different fly ashes (10 Class C and 10 Class F). PCA was used to find underlying relationships among the different elemental oxides in the fly ash particles. Next, these predicted trends were verified by making quantitative comparisons of these trends for individual particles. A grouping system was then established based on these relationships and the presence of K_2O, Na_2O, SO_3, and P_2O_5 within the particles. The contents of groups in each fly ash are then correlated with both the compressive strength and surface electrical resistivity of concretes with a 20% replacement by mass of portland cement by fly ash.

The following observations have been made:

- The following elemental oxides were found to co-exist or correlate to one another within individual fly ash particles: Na_2O and K_2O; SiO_2 and $Na_2O + K_2O$; CaO and MgO; SO_3 and P_2O_5.
- The following elemental oxides were found to not exist together or inversely correlate to one another within individual fly ash particles: CaO and $Na_2O + K_2O$; $Na_2O + K_2O$ and $SO_3 + P_2O_5$.
- Four particle groups with repeatable chemistry ranges were found in each fly ash despite the material being taken from many different sources.
- The four proposed classification groups were found in different numbers in all 20 fly ashes investigated. The relative amount of these groups are able to be used to predict the strength and resistivity of concrete mixtures with a 20% replacement by mass of the cement with fly ash.
- The simple models based on the developed grouping scheme could predict compressive strength and the electrical resistivity for concrete mixtures with 12 different fly ashes with an R^2 value of 0.96 and 0.94, respectively.

The grouping scheme established in this paper for fly ash may allow improved fly ash usage and also improve the effectiveness of the material. While more work is needed to understand why these different groups impact performance, this work provides a methodology for improving the accuracy of performance prediction of concrete containing fly ash. In addition, the fly ash particle data used in this study may give insights into the interactions between fly ash and alkali activators in alkali activated materials because the properties of alkali activated materials are also highly dependent of fly ash sources and their composition.

The methods in this paper could be used to study other types of supplementary cementitious materials and this should be investigated with future work.

Declaration of competing interest

The authors declare that they have no known competing financial interests or personal relationships that could have appeared to influence the work reported in this paper.

Acknowledgments

This work was sponsored by funding from the United States National Science Foundation CMMI 1150404 CAREER Award and by Oklahoma Transportation Center project 10.1.24.

Appendix A. Automated scanning electron microscope method (ASEM)

Initially, each fly ash was sieved to obtain 75 μm diameter and less using the No. 200 sieve. This sieving was done to prevent the large particles from skewing the bulk analysis results because one large particle can have an equal volume of thousands of small particles. The sieving process does not affect the quality of fly ash because fly ash particles are the result of the capturing process using electrostatic precipitators and filters used to separate fly ash from bottom ash. Large particles (>45 μm) generally cannot stay airborne and fall to become bottom ash. Thus most of the particles are composed of small and similar sizes of particles <75 μm. In addition, particle size distributions of unsieved C1 and C2 fly ashes were measured and compared using the ASEM technique and acoustic attenuation spectroscopy [65]. These results confirmed that the size of the majority of the particles is within the range between 30 and 50 μm [65].

Between 0.015 g and 0.018 g of the sieved material was then placed in a 50 ml polypropylene conical vial. Following this, 50 ml of a mixture of alcohol (25 ml of ethyl alcohol and 25 ml of isopropyl alcohol) was added to the vial. The vial was capped, sealed and, then sonicated for 30 min to disperse the particle and hold them in suspension. After sonicating the sample, three droplets (two to three drops using pipette) of the suspension with dispersed fly ash were placed on the double-sided adhesive carbon tape. These samples were then stored in a vacuum desiccator and the liquid was allowed to evaporate, leaving the particles on the surface of the carbon tape. These samples were stored in a vacuum desiccator until testing.

The ASEM technique was performed using the AFA equipped SEM-EDS (FEI ASPEX Explorer PSEM-EDS system). Table 3 shows the summary of the instrument settings, the scanning settings, and EDS setting used in this study. It should be noted that the constant beam performance was achieved by keeping the probe current constant with a Faraday cup and pico-ammeter. A region of interest on a sample was randomly chosen, and the particles in that field of view (81 μm × 81 μm) were screened according to pre-established requirements on their shape and size. This screening was the process to remove overlapping or touching particles from the analysis and tentatively identify foreign particles such as dust that were accidentally captured. The range of particle size that can be determined by the ASEM technique is between 0.2 μm and 50 μm. An aspect ratio of 1.3 was found to be a good parameter to search for a single fly ash particle. Each particle that meets the requirements was measured for its size, shape, perimeter, area, location, and its elemental composition using EDS.

2000 particles were selected from each fly ash (total 20 fly ashes), of which this number ensure the representative sample [28–31]. The elemental composition of each particle was then corrected by the atomic number dependent scattering, adsorption, and fluorescence effects (ZAF correction). The ZAF corrections were performed using the versatile free software called CalcZAF [28,53,54].

Appendix B. Principal component analysis of 20 fly ashes

The PCA uses a mathematical algorithm to reduce the dimensionality of the data while retaining as much information as possible [56,57]. After the PCA, the set of new variables is called the principal components (PCs) and these PCs are uncorrelated and maximize the variance of information of the raw data [56,57]. Therefore, analyzing these PCs can provide insight into the interrelationships among variables and underlying structures of the data.

For each fly ash, the original raw data obtained from the ASEM method is composed of chemical compositions of 2000 particles and each particle contains 12 compositional elemental oxide contents by mass. In other words, each fly ash data is composed of 2000 measurements and each measurement contains 12 variables.

It should be noted that the elemental oxide contents for each particle sum to a constant of 100%. Therefore, any increase in the value of a certain elemental oxide automatically requires the other elemental oxide content to decrease, demonstrating the “constant-sum constraint”. Such constrained multivariate data is not suitable for the standard multivariate statistical analyses (including the PCA) [60,61,77]. To employ the PCA using the compositional data, the appropriate transformation of the data is essential. In this paper, the centered log-ratio (clr) transformation was used because this transformation is the preferred option for compositional data [60–63]. The clr transformation is based on dividing each sample by the geometric mean of its values, and taking the logarithm as shown in Eq. (B.1). In Eq. (B.1), the D dimensional composition data $\mathbf{x} = [x_1, x_2, \ldots, x_D]$ is transformed to the data $\mathbf{y} = [y_1, y_2, \ldots, y_D]$ by the clr transformation. The clr transformed data is then used for the PCA.

$$\boldsymbol{y} = [y_1, y_2, y_3, \cdots, y_D] = \left[\ln\left(x_1 \Big/ \sqrt[D]{\Pi_{i=1}^{D} x_i}\right), \ln\left(x_2 \Big/ \sqrt[D]{\Pi_{i=1}^{D} x_i}\right), \cdots, \ln\left(x_D \Big/ \sqrt[D]{\Pi_{i=1}^{D} x_i}\right)\right] \tag{B.1}$$

The PCA generates a new set of variables called principal components (PCs), which are mathematical transformations of the original data. Each PC is the linear combination of original variables that maximize the variance among all linear combinations. This combination, thus, accounts for as much variance in the data as possible. The first PC is the best linear combination of the variables to maximize the variance of the data analyzed. The second PC is the second-best linear combination under the condition that it is orthogonal to the first PC. In this way, the variance already considered in the first PC is not accounted in the second PC. The number of PCs can be produced up to the number of variables.

After PCA, each measurement has values corresponding to new variables (PCs). These new values of PCs are called scores and these scores can be interpreted geometrically like any other data points [56,57]. In addition, the correlation coefficient between a certain principal component and a certain variable is called loading. For example, in this fly ash study, each of the 2000 measurements contained 12 elemental oxide contents. These could be expressed 2000 × 12 matrix. After PCA, a new 2000 × 12 matrix was generated and each value in the matrix is a score that was calculated using the PC loadings. The first principal component (PC1) would have 12 loadings corresponding to the 12 elemental oxides. Each of the other PCs

Table A1
Percentage of variance explained by the principal components.

Fly ash	Variance explained by PC (%)										
	PC1	PC2	PC3	PC4	PC5	PC6	PC7	PC8	PC9	PC10	Total
C1	36.2	15.9	12.6	8.1	7.3	6.1	4.9	3.6	3.4	1.9	100.0
C2	39.4	12.9	10.0	9.5	7.7	7.1	6.3	3.6	2.6	0.8	99.9
C3	39.1	12.4	11.5	10.7	7.4	5.9	4.8	3.8	2.9	1.4	100.0
C4	41.0	18.6	12.8	7.8	6.3	4.6	3.2	2.7	1.7	1.3	100.0
C5	39.1	12.4	11.5	10.7	7.4	5.9	4.8	3.8	2.9	1.4	100.0
C6	36.5	15.5	10.9	9.1	8.0	7.0	5.2	3.6	2.9	1.3	100.0
C7	44.3	13.5	10.7	8.2	6.4	5.6	4.5	3.7	1.9	1.1	100.0
C8	35.3	17.5	10.6	9.5	7.3	6.6	5.0	3.6	3.0	1.6	100.0
C9	36.4	17.2	11.4	9.0	7.4	6.7	4.4	3.8	2.7	1.0	100.0
C10	33.9	19.9	12.9	8.8	7.9	5.7	5.1	3.0	2.3	0.5	100.0
F1	37.3	14.9	12.1	9.6	8.5	5.6	4.6	3.9	2.4	1.1	100.0
F2	33.7	16.5	11.4	8.6	7.9	6.9	5.2	4.0	3.6	2.2	100.0
F3	35.5	22.1	9.3	7.9	6.8	6.1	4.9	3.1	2.8	1.5	100.0
F4	39.0	15.5	12.1	9.4	7.3	5.0	4.3	4.0	2.4	1.0	100.0
F5	29.6	21.9	11.8	11.0	8.4	6.0	4.6	3.8	1.9	1.1	100.0
F6	28.6	21.7	12.2	11.0	7.4	6.9	4.7	3.5	3.1	1.0	100.0
F7	33.6	18.7	11.5	9.5	7.5	5.7	5.2	3.9	2.9	1.4	99.9
F8	35.2	17.9	13.5	9.7	7.3	6.6	3.6	3.1	2.5	0.6	100.0
F9	39.4	13.6	12.1	8.5	8.0	6.6	4.7	2.8	2.7	1.6	100.0
F10	40.0	16.8	11.3	7.5	7.1	6.2	4.6	3.8	2.1	0.6	100.0

* Variances of PC11 and PC12 are essentially zero so they were not shown in this table.

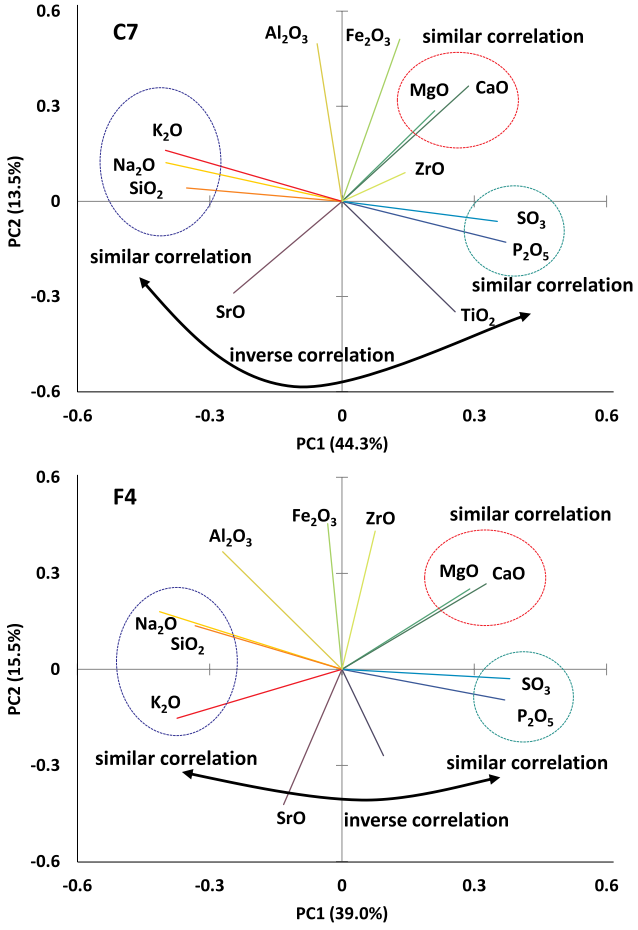

Fig. A1. Loading plots for C7 and F4, PC stands for the principal component. 'similar correlation' means that two (or more) elemental oxides tend to exist together in the same particle. 'inverse correlation' indicates that one oxide leads to suppress or decrease the content of the certain oxide in the same particle.

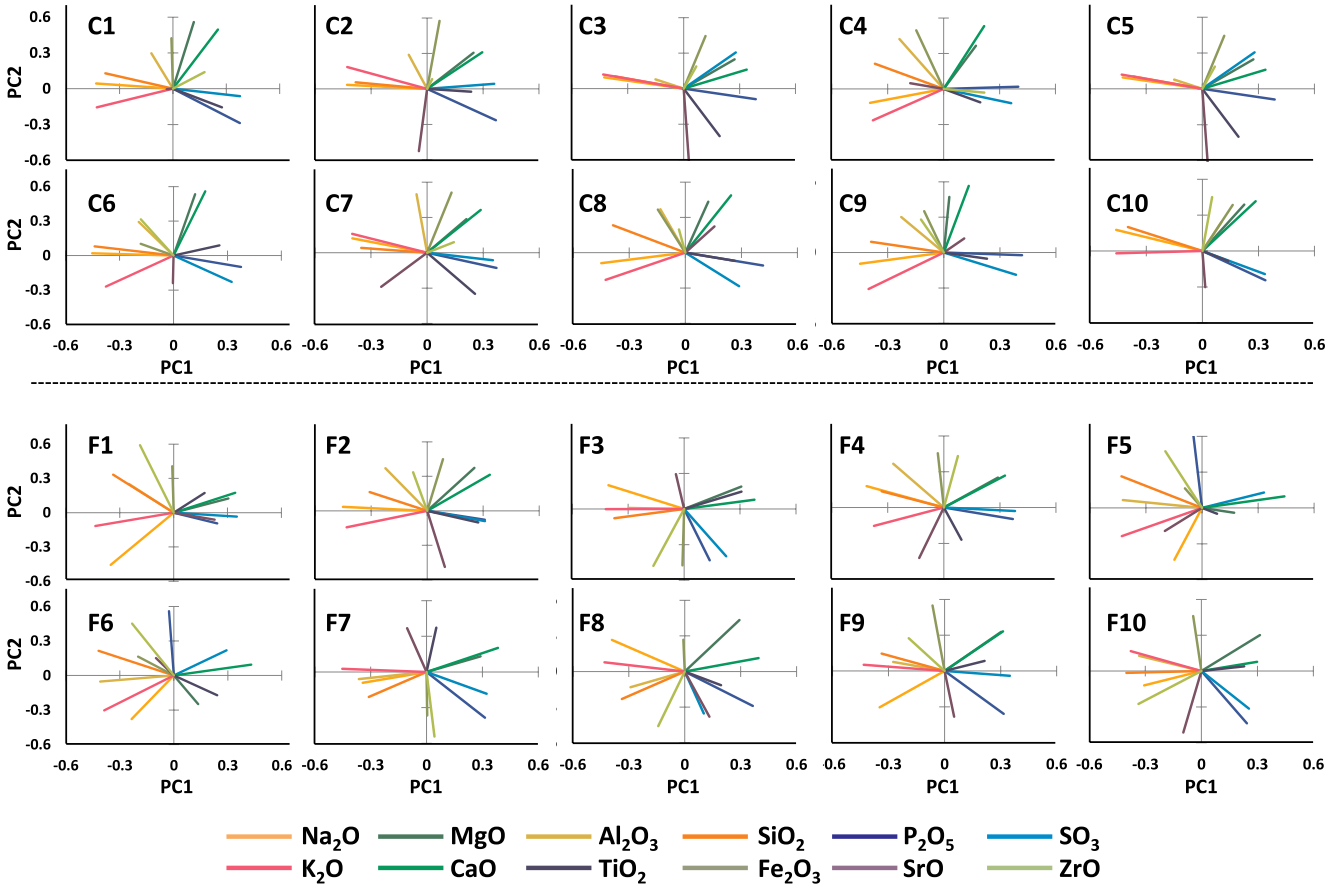

Fig. A2. Loading plots for 20 fly ashes, PC stands for the principal component. The plots are very similar. The vectors for Na_2O and K_2O, the vectors for CaO and MgO, and the vectors for SO_3 and P_2O_5 are located close together showing similar correlations. The vectors for K_2O and Na_2O are almost the opposite of CaO, showing an inverse correlation. This indicates that there are universal trends that can describe the chemical composition of the individual fly ash particles.

also has its own 12 loadings. Therefore, loadings for a PC are capable of indicating what that PC represents, and what trends of variables in the data exist [56–58]. In this paper, all the statistical calculations were performed using the statistical software R [59]. R is a highly extensible free software that provides a wide variety of statistical and graphical techniques.

The clr transformation does not allow zero values in compositional data. The zero values are rounded zeros that are below the detection limit. For this reason, a parametric zero value imputation inside the command *impRZilr* is applied to the compositional data. The clr transformation is, then, applied using the command *cenLR*. Classical PCA (using the command *PCA*) is applied to this transformed data.

Table A1 shows the variance of the data explained by the first ten principal components (PCs). It is interesting to note that the variances of the PCs for each fly ash are more or less identical. This indicates that all 20 fly ashes investigated had similar potential to be described with their PCA results. For 20 fly ashes, between 28.6% and 44.3% of the variation was described by PC1 and between 12.4% and 22.11% for PC2. This means that 20 fly ashes investigated PC1 and PC2 explained 50.2%–59.6% of the variability of the chemical composition. While including PC3 and PC4 could explain more variability, their inclusion was investigated but there were no significant findings.

To interpret the results of the PCA, the data was presented with a loading plot. Two loading plots are shown in Fig. A1 for C7 and F4. Each line is shown with a unique color and corresponds to an oxide. PC1 is shown on the x-axis and PC2 is shown on the y-axis. The variance explained by either PC1 or PC2 is shown on their respective axis.

A loading is the correlation coefficient between a certain principal component and a certain variable. Therefore, a longer or higher magnitude vector indicates that the specific oxide is well described in the corresponding PC. However, if a loading vector has a low magnitude and is close to the origin, then the specific oxide seems to be only moderately described in the corresponding PC. The direction of the vector represents the correlation between the elements. If vectors are located close to one another, that means the elements will be found to correspond to one another [57,58]. For example, in Fig. A1, the vectors for SO_3 and P_2O_5 obtained from C7 and F4 are found close to one another. This means that as one of these elements exists in a particle then so will the other. This seems to also be true for CaO and MgO from C7 and F4. In addition, SiO_2, K_2O, and Na_2O also show a correlation. Furthermore, if vectors are found in the opposite direction of one another then they will have an inverse relationship. An example of this can be seen in both plots shown in Fig. A1 as SiO_2, K_2O, and Na_2O are the opposite of SO_3 and P_2O_5. This means that in both of these fly ashes that as the amount of one of these groups exists then the amount of the other will decrease or not exist. It is important that the two plots in Fig. A1 look similar to one another. Each quadrant has more or less the same vectors for fly ash C7 and F4. These similarities suggest that there are commonalities in the elements that are found together in the analysis. This is surprising since one fly ash is a Class C and the other is a Class F and their bulk chemical compositions are very different. As can be seen from the bulk chemical composition in Table 1, the content of SiO_2 in C7 and F4 was 38.3% and 57.7% respectively. Furthermore, C7 had 21.5% CaO but F4 only had 8.1%.

The 20 individual loading plots in Fig. A2 have been plotted with the same color for each oxide so that it is easier for the reader to make quick

comparisons between the plots and quickly realize similarities and differences. The readers should realize that even though each of the plots is not exactly the same; however, the plots are very similar. For example, two green and dark green colored vectors (indicating Cao and MgO, respectively) are close to each other. Thus, CaO is similarly correlated with MgO in all 20 fly ashes. Orange (Na_2O), magenta (K_2O) and red (SiO_2) vectors are mostly close together on the right side of the axis as shown in Fig. A2. This indicates that Na_2O and K_2O and SiO_2 have a similar correlation in all 20 fly ashes. Because consistent trends are observed in all 20 fly ashes it suggests that there are universal trends that can describe the chemical composition of the individual fly ash particles for the materials investigated.

Appendix C. Validations of models

The developed models were validated using the three-fold cross-validation. The original sample (84 data) was randomly partitioned into three equal size subsamples. Two subsamples (56 samples) were used to determine the coefficients and the remaining single subsample was used as the validation data. In other words, 2/3 of the datasets are only used for fitting the parameters and 1/3 of the data is used for prediction. This three-fold validation was repeated 100 times and thus 100 sets of validation results could be obtained per each modeling (either compressive strength or surface resistivity). The statistical results of three-fold cross-validation were summarized in Table A2. It was found that the coefficient of determinants (i.e. R^2) for the compressive strength and the electrical resistivity models have small standard deviations, 0.004 and 0.001, respectively through the 100 sets of three-fold cross-validation. In addition, root means square error (RMSE) and mean absolute error (MAE) between the observed and predicted values for the cross-validations are 2.434 ± 0.093 MPa and 1.898 ± 0.081 kΩ m respectively. These small standard deviations for RMSE and MAE for 100 sets of validation indicated that the presented approach can be used for predictions with other datasets. In addition, the variation of each coefficient used in the model is summarized in Table A2. For example, the β_{s1} (the Group A coefficient for the compressive strength model) only varies within 0.242 ± 0.015 for 100 sets of the compressive strength model. Other coefficients obtained from 100 sets of three-fold cross-validation also varied within very narrow ranges, which indicates the stability and robustness of these two models. It should also be noted that the significantly small p values in Table 7 also represent the statistical robustness of the proposed approach. However, it should be noted that these models may not be applicable to other types of concrete mixtures.

Table A2
Summary of 100 sets of three-fold cross validations for compressive strength and electrical resistivity models (statistical metrics are expressed as average of 100 sets ± standard deviation).

Statistical metric		Model for compressive strength	Model for electrical resistivity
R^2		0.952 ± 0.004	0.922 ± 0.001
RMSE		2.434 ± 0.093 MPa	3.162 ± 0.128 kΩ m
MAE		1.898 ± 0.081 MPa	2.515 ± 0.087 kΩ m
Variable	**Coeff.**	**Model for compressive strength**	**Model for electrical resistivity**
Group A	β_{s1}, β_{r1}	0.242 ± 0.015	0.045 ± 0.002
Group SP	β_{s2}, β_{r2}	0.240 ± 0.009	0.000 ± 0.002
Group NASP	β_{s3}, β_{r3}	0.004 ± 0.016	0.032 ± 0.003
$\ln(t_{days})$	β_{s4}	8.285 ± 0.129	–

References

[1] R. Blissett, N. Rowson, A review of the multi-component utilisation of coal fly ash, Fuel 97 (2012) 1–23.
[2] G.G. Carette, V.M. Malhotra, Characterization of Canadian fly ashes and their relative performance in concrete, Can. J. Civ. Eng. 14 (1987) 667–682.
[3] G. Xu, X. Shi, Characteristics and applications of fly ash as a sustainable construction material: a state-of-the-art review, Resour. Conserv. Recycl. 136 (2018) 95–109.
[4] A.A. Ramezanianpour, Cement Replacement Materials, Springer-Verlag, Berlin Heidelberg, 2014.
[5] M. Ahmaruzzaman, A review on the utilization of fly ash, Prog. Energy Combust. Sci. 36 (2010) 327–363.
[6] R.S. Blissett, N.A. Rowson, A review of the multi-component utilisation of coal fly ash, Fuel 97 (2012) 1–23.
[7] K.W. Ragland, K.M. Bryden, Combustion Engineering, second ed., CRC Press, Boca Raton, FL, 2011.
[8] Z. Giergiczny, Fly ash and slag, Cement Concr. Res. 124 (2019) 105826.
[9] P. Duxson, J.L. Provis, Designing precursors for geopolymer cements, J. Am. Ceram. Soc. 91 (2008) 3864–3869.
[10] E.O. Tastan, T.B. Edil, C.H. Benson, A.M. Aydilek, Stabilization of organic soils with fly ash, J. Geotech. Geoenviron. 137 (2011) 819–833.
[11] K.H. Obla, C.L. Lob, H. Kim, The 2012 NRMCA Supplementary Cementitious Materials Use Survey, NRMCA Concrete in Focus Magazine, Silver Spring, MD, 2012, pp. 16–18.
[12] R.J. Flatt, N. Roussel, C.R. Cheeseman, Concrete: an eco material that needs to be improved, J. Eur. Ceram. Soc. 32 (2012) 2787–2798.
[13] M.J. McCarthy, R.K. Dhir, Development of high volume fly ash cements for use in concrete construction, Fuel 84 (2005) 1423–1432.
[14] M.H. Zhang, Canmet, Microstructure, crack propagation, and mechanical properties of cement pastes containing high volumes of fly ashes, Cement Concr. Res. 25 (1995) 1165–1178.
[15] R. Siddique, Performance characteristics of high-volume Class F fly ash concrete, Cement Concr. Res. 34 (2004) 487–493.
[16] V.M. Malhotra, Durability of concrete incorporating high-volume of low-calcium (ASTM Class F) fly ash, Cement Concr. Compos. 12 (1990) 271–277.
[17] R. Kurda, J. de Brito, J.D. Silvestre, Combined influence of recycled concrete aggregates and high contents of fly ash on concrete properties, Constr. Build. Mater. 157 (2017) 554–572.
[18] R. Kurda, J.D. Silvestre, J. de Brito, H. Ahmed, Optimizing recycled concrete containing high volume of fly ash in terms of the embodied energy and chloride ion resistance, J. Clean. Prod. 194 (2018) 735–750.
[19] H.S. Pietersen, A.L.A. Fraay, J.M. Bijen, Reactivity of fly ash at high pH, in: Materials Research Society Symposium Proceedings, 1990.
[20] G.J. McCarthy, K.D. Swanson, L.P. Keller, W.C. Blatter, Mineralogy of western fly ash, Cement Concr. Res. 14 (1984) 471–478.
[21] R.T. Chancey, P. Stutzman, M.C.G. Juenger, D.W. Fowler, Comprehensive phase characterization of crystalline and amorphous phases of a Class F fly ash, Cement Concr. Res. 40 (2010) 146–156.
[22] S.K. Das, Yudhbir, A simplified model for prediction of pozzolanic characteristics of fly ash, based on chemical composition, Cement Concr. Res. 36 (2006) 1827–1832.
[23] S.C. White, E.D. Case, Characterization of fly ash from coal-fired power plants, J. Mater. Sci. 25 (1990) 5215–5219.
[24] S. Diamond, On the glass present in low-calcium and in high-calcium fly ashes, Cement Concr. Res. 13 (1983) 459–464.
[25] L. Du, E. Lukefahr, A. Naranjo, Texas department of fly ash database and the development of chemical composition-based fly ash alkali-silica reaction durability index, J. Mater. Civ. Eng. 25 (2013) 70–77.
[26] ASTM C618 - Standard Specification for Coal Fly Ash and Raw or Calcined Natural Pozzolan for Use in Concrete, American Society for Testing and Materials, West Coshonhocken, PA, 2014.
[27] BS EN 450-1, Fly Ash for Concrete. Definition, Specification and Conformity Criteria, British Standards Institution, 2012.
[28] M. Aboustait, T. Kim, M.T. Ley, J.M. Davis, Physical and chemical characteristics of fly ash using automated scanning electron microscopy, Constr. Build. Mater. 106 (2016) 1–10.

[29] T. Kim, J.M. Davis, M.T. Ley, S. Kang, Fly ash particle characterization for predicting concrete compressive strength, Constr. Build. Mater. 165 (2018) 560–571.
[30] T. Kim, M. Moradian, M.T. Ley, Dissolution and leaching of fly ash in nitric acid using automated scanning electron microscopy, Adv. Civil Eng. Mater. 7 (2018) 291–307.
[31] T. Kim, Q. Hu, M.T. Ley, M. Aboustait, J. Bullard, Using particle characterization to study fly ash dissolution and leaching in water and KOH solution, ACI Mater. J. 116 (4) (2019) 5–17.
[32] S.V. Vassilev, R. Menendez, D. Alvarez, M. Diaz-Somoano, M.R. Martinez-Tarazona, Phase-mineral and chemical composition of coal fly ashes as a basis for their multicomponent utilization. 1. Characterization of feed coals and fly ashes, Fuel 82 (2003) 1793–1811.
[33] P.T. Durdziński, C.F. Dunant, M.B. Haha, K.L. Scrivener, A new quantification method based on SEM-EDS to assess fly ash composition and study the reaction of its individual components in hydrating cement paste, Cement Concr. Res. 73 (2015) 111–122.
[34] Q. Hu, M.T. Ley, J. Davis, J.C. Hanan, R. Frazier, Y. Zhang, 3D chemical segmentation of fly ash particles with X-ray computed tomography and electron probe microanalysis, Fuel 116 (2014) 229–236.
[35] Q. Hu, M. Aboustait, M.T. Ley, J.C. Hanan, V. Rose, R. Winarski, Combined three-dimensional structure and chemistry imaging with nanoscale resolution, Acta Mater. 77 (2014) 173–182.
[36] B.G. Kutchko, A.G. Kim, Fly ash characterization by SEM–EDS, Fuel 85 (2006) 2537–2544.
[37] K.L. Aughenbaugh, R.T. Chancey, P. Stutzman, M.C. Juenger, D.W. Fowler, An examination of the reactivity of fly ash in cementitious pore solutions, Mater. Struct. 46 (2012) 869–880.
[38] P.T. Durdziński, R. Snellings, C.F. Dunant, M.B. Haha, K.L. Scrivener, Fly ash as an assemblage of model Ca–Mg–Na-aluminosilicate glasses, Cement Concr. Res. 78 (2015) 263–272. Part B.
[39] M. Aboustait, Multi-scale Analytical Investigation of Fly Ash in Concrete, Civil and Environmental Engineering, Oklahoma state university, Stillwater, OK, 2015, p. 238.
[40] M. Aboustait, Q. Hu, R. Frazier, Y. Zhang, B. Tabb, T. Ley, J. Hanan, Innovative Prediction of Fly Ash Performance in Concrete, Oklahoma Transportation Center, 2013, p. 78.
[41] V.V. Kindratenko, P.J.M. Van Espen, B.A. Treiger, R.E. Van Grieken, Fractal dimensional classification of aerosol particles by computer-controlled scanning electron microscopy, Environ. Sci. Technol. 28 (1994) 2197–2202.
[42] S. Ghosal, J.L. Ebert, S.A. Self, Chemical composition and size distributions for fly ashes, Fuel Process. Techonol. 44 (1995) 81–94.
[43] Y. Chen, N. Shah, F.E. Huggins, G.P. Huffman, W.P. Linak, C.A. Miller, Investigation of primary fine particulate matter from coal combustion by computer-controlled scanning electron microscopy, Fuel Process. Techonol. 85 (2004) 743–761.
[44] A. Laskin, J.P. Cowin, M.J. Iedema, Analysis of individual environmental particles using modern methods of electron microscopy and X-ray microanalysis, J. Electron. Spectrosc. Relat. Phenom. 150 (2006) 260–274.
[45] AASHTO T 358 - Method of Test for Surface Resistivity Indication of Concrete's Ability to Resist Chloride Ion Penetration, American Associaton of State Highway and Transportation Officials, Washington DC, 2015.
[46] ASTM D4326 - 13, Standard Test Method for Major and Minor Elements in Coal and Coke Ash by X-Ray Fluorescence, American Society for Testing and Materials, West Coshonhocken, PA, 2014.
[47] R.P. Gupta, T.F. Wall, I. Kajigaya, S. Miyamae, Y. Tsumita, Computer-controlled scanning electron microscopy of minerals in coal—implications for ash deposition, Prog. Energy Combust. Sci. 24 (1998) 523–543.
[48] C.A. O'Keefe, T.M. Watne, J.P. Hurley, Development of advanced scanning electron microscopy techniques for characterization of submicron ash, Powder Technol. 108 (2000) 95–102.
[49] J. Armstrong, Quantitative elemental analysis of individual microparticles with electron beam instruments, in: K.F.J. Heinrich, D. Newbury (Eds.), Electron Probe Quantitation, Springer US, 1991, pp. 261–315.
[50] G. Love, V.D. Scott, Evaluation of a new correction procedure for quantitative electron probe microanalysis, J. Phys. D Appl. Phys. 11 (1978) 1369–1376.
[51] J.T. Armstrong, P.R. Buseck, Quantitative chemical analysis of individual microparticles using the electron microprobe, Theor. Anal. Chem. 47 (1975) 2178–2192.
[52] J.T. Armstrong, P.R. Buseck, A general characteristic fluorescence correction for the quantitative electron microbeam analysis of thick specimens, thin films and particles, X Ray Spectrom. 14 (1985) 172–182.
[53] J.T. Armstrong, J.J. Donovan, P.C. Carpenter, CALCZAF, TRYZAF and CITZAF: the use of multi-correction-algorithm programs for estimating uncertainties and improving quantitative X-ray analysis of difficulty specimens, Microsc. Res. Tech. 19 (suppl. 2) (2013) 812–813.
[54] Available on the internet, CalcZAF, http://epmalab.uoregon.edu/calczaf.htm.
[55] H.M. Storms, K.H. Janssens, S.B. Török, R.E. Van Grieken, Evaluation of the armstrong–buseck correction for automated electron probe X-ray microanalysis of particles, X Ray Spectrom. 18 (1989) 45–52.
[56] I.T. Jolliffe, Principal Component Analysis, second ed., Springer, New York, 2002.
[57] R. Bro, A.K. Smilde, Principal component analysis, Anal. Method 6 (2014) 2812–2831.
[58] H. Abdi, L.J. Williams, Principal component analysis, Wiley Interdiscip. Rev. Comput. Stat. 2 (2010) 433–459.
[59] R development core team, available on the internet, http://www.r-project.org/.
[60] J. Aitchison, The statistical analysis of compositional data, J. R. Stat. Soc. Ser. B 44 (1982) 139–177.
[61] J. Aitchison, Reducing the dimensionality of compositional data sets, J. Int. Assoc. Math. Geol. 16 (1984) 617–635.
[62] J. Aitchison, Principal component analysis of compositional data, Biometrika 70 (1983) 57–65.
[63] J. Aitchison, M. Greenacre, Biplots of compositional data, J. R. Stat. Soc. Ser. C Appl. Stat. 51 (2002) 375–392.
[64] ASTM C39 - Standard Test Method for Compressive Strength of Cylinderical Concrete Specimens, American Society for Testing and Materials, West Coshonhocken, PA, 2016.
[65] C.P. Aichele, D. Venkataramani, J.E. Smay, M.H. McCann, S. Richter, M. Khanzadeh-Moradllo, M. Aboustait, M.T. Ley, A comparison of automated scanning electron microscopy (ASEM) and acoustic attenuation spectroscopy (AAS) instruments for particle sizing, Colloid. Surf. Physicochem. Eng. Asp. 479 (2015) 46–51.
[66] K.R. Gabriel, The biplot graphic display of matrices with application to principal component analysis, Biometrika 58 (1971) 453–467.
[67] K. Hron, M. Jelínková, P. Filzmoser, R. Kreuziger, P. Bednář, P. Barták, Statistical analysis of wines using a robust compositional biplot, Talanta 90 (2012) 46–50.
[68] P.G.A.R.A. Hamed Layssi, S. Mustafa, Electrical resistivity of concrete, Concr. Int., 37.
[69] ASTM C1585 - Standard Measurement of Rate of Absorption of Water by Hydraoulic Cement Concrete, American Society for Testing and Materials, West Coshonhocken, PA, 2014.
[70] F. Hunkeler, The resistivity of pore water solution—a decisive parameter of rebar corrosion and repair methods, Constr. Build. Mater. 10 (1996) 381–389.
[71] K.A. Snyder, X. Feng, B.D. Keen, T.O. Mason, Estimating the electrical conductivity of cement paste pore solutions from OH−, K+ and Na+ concentrations, Cement Concr. Res. 33 (2003) 793–798.
[72] I. Suarez-Ruiz, C.R. Ward, Coal combustion, in: I. Suarez-Ruiz, J.C. Crelling (Eds.), Applied Coal Petrology: the Role of Petrology in Coal Utilizatoin, first ed., Academic Press, 2008, pp. 85–117.
[73] I. Suarez-Ruiz, C.R. Ward, Basic factors controlling coal quality and technological behavior, in: I. Suarez-Ruiz, J.C. Crelling (Eds.), Applied Coal Petrology: the Role of Petrology in Coal Utilizatoin, first ed., Academic Press, 2008, pp. 19–59.
[74] R.A. Creelman, C.R. Ward, G. Schumacher, L. Juniper, Relation between coal mineral matter and deposit mineralogy in pulverized fuel furnaces, Energy Fuels 27 (2013) 5714–5724.
[75] B.J.P. Buhre, J.T. Hinkley, R.P. Gupta, P.F. Nelson, T.F. Wall, Fine ash formation during combustion of pulverised coal–coal property impacts, Fuel 85 (2006) 185–193.
[76] C. Ward, C. Heidrich, O. Yeatman, Coal Combustion Products Handbook, second ed., Ash Development Association of Australia, 2014.
[77] F. Chayes, On correlation between variables of constant sum, J. Geophys. Res. 65 (1960) 4185–4193.